Article

Comparative Analysis of Electrospun Silk Fibroin/Chitosan Sandwich-Structured Scaffolds for Osteo Regeneration: Evaluating Mechanical Properties, Biological Performance, and Drug Release

Rama Murugapandian, Sundara Ganeasan Mohan, Sridhar T M, N. Arunai Nambi Raj, and Vijayalakshmi Uthirapathy*

Cite This: ACS Omega 2024, 9, 28072−28092

Read Online

ACCESS | Metrics & More | Article Recommendations | Supporting Information

ABSTRACT: An intensive idea of bone tissue engineering is to design regenerative nanofibrous scaffolds that could afford a natural extracellular matrix (ECM) microenvironment with the ability to induce cell proliferation, biodegradation, sustained drug release, and bioactivity. Even the mechanical properties and orientation of the nanofibers may enhance the performance of the scaffolds. To address this issue, we designed novel sandwich-like hybrid silk fibroin (SF)/silica/poly(vinyl alcohol) (PVA) nanofibers scaffolds. The developed scaffold was further characterized using scanning electron microscopy (SEM), elemental mapping, X-ray diffraction (XRD), Fourier-transform infrared (FTIR), and water/blood contact angle measurements. Owing to the interfacial interaction between the layers of organic (chitosan/silk fibroin) and inorganic (silica) in the nanofibrous scaffold, a biocompatibility study has been made on an osteoblast-like (MG63) cell line, which has significant statistical differences; hemocompatibility and the mechanical profile were evaluated in detail to understand the suitability as a biomaterial. To endow the scaffold biodegradation rate, antibacterial activity, porosity profile, and cephalexin monohydrate (CEM), a drug-loading/drug release study was also performed for all of the nanofibers. This strategy explored superior mechanical strength with higher biomineralization on SF/silica/PVA nanofibers. Eventually, the proposed article compared the observation of monolayered scaffolds with designed sandwich-structured scaffolds for the enhancement of bone regeneration.
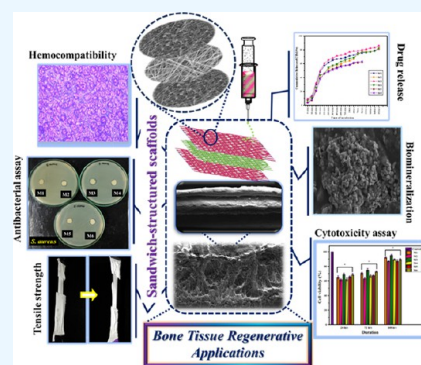
1. INTRODUCTION

The strategy of bone tissue engineering (BTE) seeks to create an implantable bone substitute with osteogenic properties for critical skeletal defects in orthopedics. The most common bone defects are osteogenesis, osteoporosis, osteoarthritis, osteomyelitis, etc. Among recent investigations, autogenic/allogenic cells, biomaterials, and or combinations thereof have been used to rectify the challenges in BTE.[1,2] Matsubara et al. developed a porous hydroxyapatite/collagen combined with autologous blood, which is rich in growth factors to promote bone fusion.[3] Autogenous bone grafts are the best choice for repairing a high rate of bone-defected sites due to their osteoinductive and osteoconductive capacity. However, the grafting shows certain limitations and complications during post-transplantations. This challenge prompted the search for bone augmentation using the ideal synthetic materials. An array of biomaterials holds greater potential for osteoinductive property in the designed matrices (scaffolds or Supporting Material).[4]

Scaffold-based materials are considered to be a biomimetic approach, which uses various polymers such as polylactic acid (PLA), poly(vinyl alcohol) (PVA), poly(lactic-*co*-glycolic acid) (PLGA), gelatin, chitosan, starch, etc., proteins (silk fibroin, soy, collagen), and bioceramics/bioglass (Hydroxyapatite

(HAP), β-TCP, silica, etc.,).[5] Concerning biocompatible polymers, PVA can carry and release drug/biological molecules like protein. PVA also forms a fibrous network mat, which facilitates its high tensile strength.[6] Silk fibroin (SF) is a well-known fibrous protein that contains a sequence of amino acids (hexapeptides and dipeptides) that forms a more stable antiparallel β-sheet crystalline structure. This β-sheet conformation contributes to slow degradation during regeneration and increases the mechanical potential of the bone scaffolds. Nonetheless, SF has gained remarkable characteristics in terms of biocompatibility and biodegradation; it shows low osteogenic capacity in the orthopedic arena unless it is functionalized.[7] Chitosan, a carbohydrate biopolymer with glycosaminoglycans (GAG) and glycosidic linkage $(1 \rightarrow 4)$ has excellent antibacterial activity, stimulates the healing process, is hemostatic, has the ability to enhance biofunctions of the

Table 1. Composition of the Outer Layer and the Middle Layer of the Sandwich-Layered Scaffolds

sample code	outer layer composition (top and bottom)	middle layer composition
M1	PVA + silk fibroin (SF)	PVA + silica (SiO_2)
M2	PVA + silica (SiO_2)	PVA + silk fibroin (SF)
M3	PVA + silk fibroin (SF) + chitosan (CS)	PVA + silica (SiO_2)
M4	PVA + silica (SiO_2)	PVA + silk fibroin (SF) + chitosan (CS)

scaffolds, and has a bacteriostatic property, and has a high swelling property. It has been reported that the addition of chitosan may decrease the porosity by lowering the mechanical strength until it is functionalized with other components.[8]

To date, there are various techniques available for developing desired scaffolds for targeting defects in bone tissue engineering (BTE). The most fabricating methods are electrospinning, solvent casting particulate leaching, freeze-drying, gas foaming, and thermal-induced phase separation.[9] The architecture of scaffolds with porous topography, high surface area, and fiber dimensions down to the nanometer range provides both soft and hard tissue regenerative applications. Hence, among other methods, electrospinning is a pioneering technique in nanotechnology, which can provide spiral fibers with a nanoscale diameter for directing cellular response during the regeneration process/reconstruction of bone defects. Further, a huge surface area merely favors cell proliferation compared with other conventional methods for a wide range of biomedical applications.[10,11]

Silica (polycrystalline ceramic glass) has good osteoconductive properties and the ability to form new bone tissue and is widely used in bone tissue engineering. Silica-based nanofibers can effectively deliver antibiotics by forming an integrin−ligand interaction to stimulate regeneration.[12,13] In this study, we have reported sandwich-structured multifunctional layers composed of silica nanoparticles ($nSiO_2$) combined with a polymeric phase (PVA, silk fibroin, and chitosan). Silica has a surface affinity toward silk fibroin, which would decorate the inner and outer layers of "sandwich-like matrices". Recently, Zhang et al. reported a multifunctional kartogenin-loaded hydroxyapatite/polycaprolactone bilayered osteogenic scaffold modified with tannic acid (as a prime coating for surface modification) and peptide conjunction implanted in the rabbit model. His study anticipated that the layered multifunctional scaffolds could effectively improve osteochondral regeneration for cartilage repair. Besides, our previous study has investigated a different concentration of cephalexin monohydrate (CEM)-loaded sandwich-layered scaffolds to effectively promote regeneration and supports infection control by steady sustained release of drugs.[14]

Nanofibrous scaffolds mimic the extracellular matrix of natural bone tissues;[15] however, the sandwich-like structure (i.e., incorporating different compositions or functionalities of layers) can offer a high surface area, porosity, cell infiltration, and nutrient exchange. The requirement of a scaffold for bone regeneration is complex; hence, multilayer scaffolds can improve the stability of the scaffold to achieve the gradual release of drug molecules compared to monolayer scaffolds. This present work proposes a different organic (silk fibroin/chitosan)−inorganic (silica) matrix to mimic the bone tissue, improve mechanical properties, gradual degradation over new bone formation, prevent stress shielding, and support controlled delivery. Wang et al. anticipated that sandwich structure nanofibers enhanced robust hydrogen bonding, electrostatic interactions, and van der Waals interactions

between composite substrates.[16] Yahia et al. reported that chitosan-based sandwich-like nanofibrous scaffolds improved the bioactivity, angiogenesis, proliferation of osteoblast cells, tensile strength, and the matrix tend to mimic organic components of bone extracellular matrix (ECM) to improve cell−cell/cell−matrix intercommunications.[17] Recently, Wang et al. proposed sandwich-like nanofibers loaded with naringenin/vitamin K for bone repair defects, offering a microenvironment for cell growth and proliferation of bone cells.[18]

In our previous finding, we reported novel sandwich-layered silver-doped mesoporous silica nanofibers stuffed with antibiotic drugs to induce synergistic action against microbial growth.[19] However, in this current study, we have investigated the effect of embedding silica nanoparticles/silk fibroin and chitosan-based hydrophilic nanofibrous scaffolds for better osteogenic differentiation of osteoblast cells. Moreover, this study compares the effective use of sandwich-layered with monolayered scaffolds and the effect of chitosan and cephalexin monohydrate (CEM, an antibiotic drug) loading/releasing efficacy of the composite scaffolds. Taken together, the outcome results signposted that the multifunctional "sandwich-structured" nanofiber could offer a promising scaffold for bone tissue engineering with prolonged drug delivery applications.

2. EXPERIMENTAL SECTION

2.1. Materials. Tetraethyl orthosilicate, TEOS, and poly-(vinyl alcohol) ((PVA) average molecular weight of 50,000−125,000) were supplied by Sigma-Aldrich. *Bombyx mori* silk cocoons were purchased from the local market, and dialysis tube-70 was obtained from HIMEDIA (India). Calcium chloride ($CaCl_2$), ethanol, and sodium carbonate (Na_2CO_3) were purchased from SDFCL (SD FINE-CHEM LIMITED, India).

2.2. Methods. *2.2.1. Synthesis of Silica Nanoparticles.* The silica (SiO_2) powder was prepared with tetraethyl orthosilicate (TEOS) and nitric acid/acetic acid as precursors. Subsequently, 6.4 mL of deionized water and 18 mL of TEOS were mixed and stirred continuously for 10 min. Then, 36 mL of nitric acid/acetic acid was added dropwise to the solution, followed by stirring for 1.5 h. The obtained gel was dried at 80 °C for 2 h and then sintered at 600 °C for 2 h.

2.2.2. Extraction of Silk Fibroin from Cocoons. B. mori silk cocoons were cut into small pieces, according to the protocol reported earlier.[20] Briefly, the dried cocoon pieces were boiled in 0.02 M Na_2CO_3 for 30 min to soften the water-soluble sericin protein. The degummed fiber mass was rinsed, squeezed out with an excess of water, and allowed to dry overnight in a hot air oven. The obtained fiber was then dissolved in the $CaCl_2/C_2H_5OH/H_2O$ system at 80 °C for 2 h. The dissolved solution was dialyzed against ultrapure water for 48 h. After dialysis, the solution was centrifuged and stored at 4 °C for further experiment.
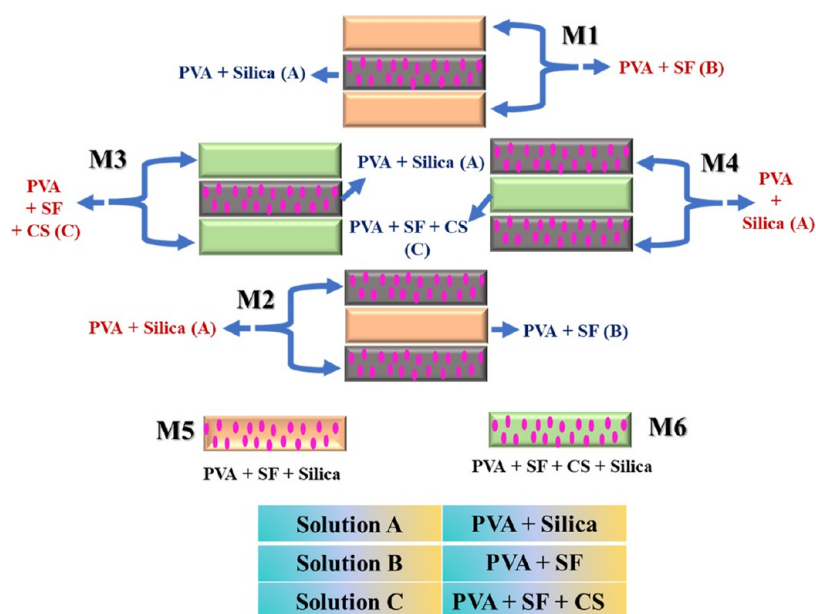
Figure 1. Assembly of sandwich-structured nanofibrous scaffolds M1, M2, M3, and M4 and monolayered nanofibers M5 and M6 with same diameter thickness by using the electrospinning technique.

2.2.3. Preparation of a Spinning Solution. The spinning medium, poly(vinyl alcohol) (PVA), was dissolved in hot water and stirred for complete dissolution. Prepared SiO_2 powder was added to PVA (solution A, SiO_2 + PVA), and concentrated SF was added along with the PVA solution in another beaker (solution B, SF + PVA). Chitosan (CS) was dissolved in acetic acid (2%) and added in a separate beaker (solution C, having the composition of SF + CS + PVA) along with the addition of SF/PVA. These solutions were allowed to be stirred overnight for complete blending. The spinning solutions (A–C, also illustrated in Table 1) were loaded in a 5 mL syringe with an applied high voltage of 18–20 kV. The distance between the collector and the capillary tip was about 15 cm. The flow rate of the solution was kept at 1 mL/h, and fibers were collected according to a design of sandwich-like layers (schematically represented in Figure 1).

2.3. Analytical Methods. *2.3.1. FTIR Analysis and In Silico Docking.* Functional groups of the surface of the sandwich-like scaffold were analyzes using an IR Affinity-1 Fourier Transform infrared spectrometer, FTIR (SHIMAD-ZU), in the spectral region of 400–4000 cm^{-1}. The spectra were recorded from 21 scan signal-averaged with a resolution of 4 or 8 cm^{-1}.

2.3.2. XRD Analysis. The X-ray diffraction (XRD) pattern of sandwich-like scaffolds was recorded on a SHIMADZU X-ray diffractometer (model Lab XRD−600) composed of a Cu Kβ radiation (λ = 1.5418 Å) source at 40 kV and 30 mA, from the 2θ range of 0–90° at a scanning speed of 10°/min.

2.3.3. SEM/EDAX Analysis. The cross-sectional view and top-view morphologies of the fabricated sandwich-type scaffolds were observed via scanning electron microscopy (SEM) (JSM-5610LV, JEOL). To observe the network morphologies of scaffolds, the fibers were cut into squares of 1 cm × 1 cm gold-coated at an accelerating voltage of 10 kV. The elemental analysis was carried out by an energy-dispersive X-ray analyzer (EDAX) (INCA, oxford instrument), which was directly connected to SEM, and the environmental mode was the same as that of SEM observations (SEM-EDAX). The

average fiber diameter was measured using ImageJ analysis and calculated from SEM micrographs by selecting 50 nanofibers.

2.3.4. In Vitro Bioactivity Test. Assessment of the mineralization process on the sandwich-type nanofibers was investigated in a freshly simulated body fluid (SBF, prepared using the standard procedure by Kokubo et al.)[21] solution at a pH of 7.4. A small piece of the sample was soaked in an SBF solution (20 mL) and replaced every 24 h for 7 and 14 days. After specimens were removed from the SBF solution at incubation time intervals, the scaffolds were rinsed in deionized water and dried in an oven for further analysis. The scaffolds were then sectioned and evaluated by FTIR, XRD, and SEM, respectively.

2.3.5. Wettability of Water (WCA) and the Blood Contact Angle (BCA). The static water contact angle and the blood contact angle on sandwich-like nanofibers were measured using the GBX instrument (Germany at 25 °C). At first, the samples were cut into 2 cm × 2 cm sizes, dried, and pressured to obtain a dense top surface to avoid the capillary penetration effect. Blood considered for this experiment was human blood taken from a healthy volunteer and added with a pinch of EDTA. The blood solution and milli-Q water with a volume of about 2 μL were dropped on the sample surface, and a picture of the drop was captured from a sessile drop by using a syringe. The angles of the sessile drop were measured at three different locations for each membrane, and the average value of the angle at the liquid−solid interface was measured.

2.3.6. Degradation Property and Porosity of Sandwich-Type Nanofibers. The degradation property and porosity of sandwich-type nanofibers were evaluated in an SBF solution (Hank's solution) at a pH of 7.4. The scaffolds were soaked in the SBF solution at 37 °C for 3, 7, 14, 21, and 28 days, respectively. After the scheduled time, the immersed scaffolds were gently rinsed in distilled water and dehydrated at 60 °C, with the final weight of each sample being accurately measured. The percentage of the retained mass of the sandwich-type scaffolds (rate of degradation) was calculated using the following formula[22]

$$\text{weight loss of the scaffold (\%)} = \frac{(W_i - W_f)}{W_i} \times 100 \qquad (1)$$

where W_i is the initial dry weight of the scaffold and W_f is the final dry weight of the scaffold after degradation.

The porosity of the sandwich-type nanofibers was measured using the liquid intrusion method. Briefly, the sandwich-type nanofibers were weighed and immersed in 100% ethanol for 48 h at room temperature. The porosity of the scaffolds was calculated using the following formula[23]

$$\text{porosity of the scaffold (\%)} = \frac{(S_2 - S_1)}{pV} \times 100 \qquad (2)$$

where S_2 is the weight of the scaffold immersed in ethanol, S_1 is the weight of the dry scaffold before immersion, p is the density of the ethanol, and V is the total volume of the sandwich scaffolds with intruded ethanol ($n = 5$).

2.3.7. Mechanical Property. The mechanical properties of the scaffolds were analyzed to evaluate mechanical forces under the biophysical environment of a natural bone. Tensile strength for electrospun nanofibers was performed using an ASTM standard (D695) on the Tinus Olsen H5K5 universal testing machine. Nanofibers were cut into a rectangular shape of width 12 mm and placed at a height of 6 cm between two clamps bearing a 500N load cell with a velocity of 1 mm/min. The average of three trials of the tensile modulus was calculated from the stress−strain response.

2.3.8. Hemocompatibility of Nanofibers. The hemocompatibility of the monolayer and sandwich-type electrospun nanofibrous membranes was examined using the guidelines of ASTM F 756-00. The samples were cut into 10 mm × 10 mm in area and sterilized in a physiological saline solution at normal body temperature for 30 min, followed by centrifugation to prepare the test extract. Human blood was drawn from a healthy adult volunteer (ref.no.VIT/IECH/XIII/2023/17), approved by the Institutional Ethical Committee for Studies on Human subjects (IECH), and collected with an anticoagulant and was further diluted with sterilized saline, where the saline was taken as negative control countering distilled water with a positive control. The test solution was incubated at the body temperature (37 °C) for 30 min. After the incubation, the extract of samples was collected by centrifugation (3000 rpm), and the absorbance at 545 nm of each supernatant was determined by a ultraviolet (UV)−visible scanning spectrophotometer (Shimadzu UV-1800). The hemolysis ratio (HR) was calculated by using the formula:[24]

$$HR = \frac{D_t - D_{nc}}{D_{pc} - D_{nc}} \times 100\% \qquad (3)$$

where HR is the hemolysis ratio and D_t, D_{nc}, and D_{pc} are average absorbance values of the respective sample, negative control, and positive control, respectively. Triplicate values were recorded to avoid any discrepancy, and the standard deviations were plotted as errors. Hemolytic grades are determined as nonhemolytic for HR values between 0 and 2, 2 and 5 as slight hemolytic, and hemolytic for above 5 units.

2.3.9. Antibacterial Analysis. The antibacterial efficacy of the samples was evaluated by the disc diffusion method in terms of the inhibition zones. Nanofibers were cut into small pieces and sterilized before microbiological studies. Common human pathogens *Staphylococcus aureus* (Gram-positive) and *Escherichia coli* (Gram-negative) were cultured over Petri plates over a standard agar growth medium via the spread plate technique. The nanofibers were placed over the culture when semidried and incubated in a CO_2 incubator with appropriate moisture content for 24 h at 37 °C. After incubation, the images of a respective zone of inhibition were recorded to elucidate the antibacterial properties of the samples.

2.3.10. In Vitro Cytocompatibility Studies. The osteoblast-like (MG63) cell line was plated separately and cultivated using 96-well plates with a concentration of 1×10^4 cells/well in DMEM supplemented with a 1× antibiotic antimycotic solution and 10% fetal bovine serum (Himedia, India) at 37 °C with a 5% CO_2 atmosphere. The cells were washed with 200 μL of 1× phosphate-buffered saline (PBS), and then the cells were treated with various test concentrations of the synthesized material in serum-free media and were incubated for 24 h. The medium was aspirated from cells at the end of the treatment period. Then, 0.5 mg/mL MTT prepared in 1× PBS was added and incubated at 37 °C for 4 h using a CO_2 incubator. After the incubation period, the medium containing MTT was discarded from the cells and washed using 200 μL of PBS. The formed crystals were dissolved with 100 μL of DMSO and thoroughly mixed. The color exchange was evaluated by the absorbance at 570 nm using a microplate spectrophotometer.[25]

2.3.11. In Vitro Drug-Loading Efficiency and Drug Release. One milligram/milliliter of the drug (cephalexin monohydrate, an antibacterial drug) was loaded into the scaffolds, and the concentration of the drug was determined using a UV−visible spectrophotometer (JASCO UV−visible spectrometer) at 200−400 nm. The fibrous membranes were sectioned into 1×1 cm^2 and weighed before incubation at 37 °C in phosphate-buffered saline (PBS, pH 7.4 ± 0.1). These scaffolds were placed in a beaker containing a PBS medium on an orbital shaker rotator at 120 rpm. The resulting elution fluids were collected to calculate the drug-loading and drug releasing efficiency by plotting absorption against the wavelength for different time intervals. The cumulative drug release was calculated every 30 min for 2, 4, 6, 8, 10, 12, 24, 48, 72, 96, 120, 144, 168, and 192 h, respectively. The loading efficiency in the aqueous medium and cumulative release in percentage[26] were calculated in triplicate using the formula mentioned below

$$\begin{aligned}&\text{drug loading efficiency (\%)} \\ &= \frac{\text{initial conc} - \text{final conc}}{\text{initial conc}} \times 100\%\end{aligned} \qquad (4)$$

3. RESULTS AND DISCUSSION

3.1. Selection of the Catalyst for the Preparation of Silica for Sandwich-Structured Nanofibers. Solvents such as nitric and acetic acids were selected as catalysts in the synthesis of silica particles using the sol−gel method via an acid-catalyzed hydrolysis process. During this process, tetraethyl orthosilicate $[Si−(OC_2H_5)_4]$ undergoes hydrolysis, catalyzed by the nucleophilic attack of oxygen from water (O−H) molecules on a silicon atom, resulting in the formation of silanol groups via bimolecular nucleophilic displacement (S_N2 mechanism). In an acidic medium (e.g., nitric acid and acetic acid), protonation of the alkoxyl group occurs by making the silicon atom more electrophilic, which then attacks the nucleophilic oxygen atom. Subsequently, the condensation process can occur either by alcohol or water to generate
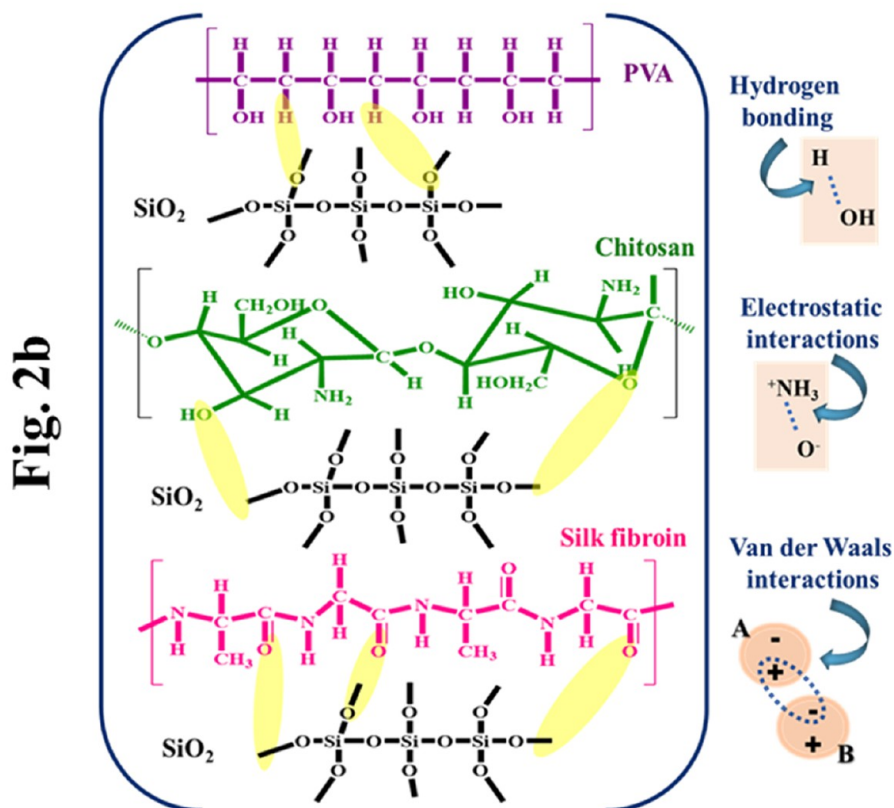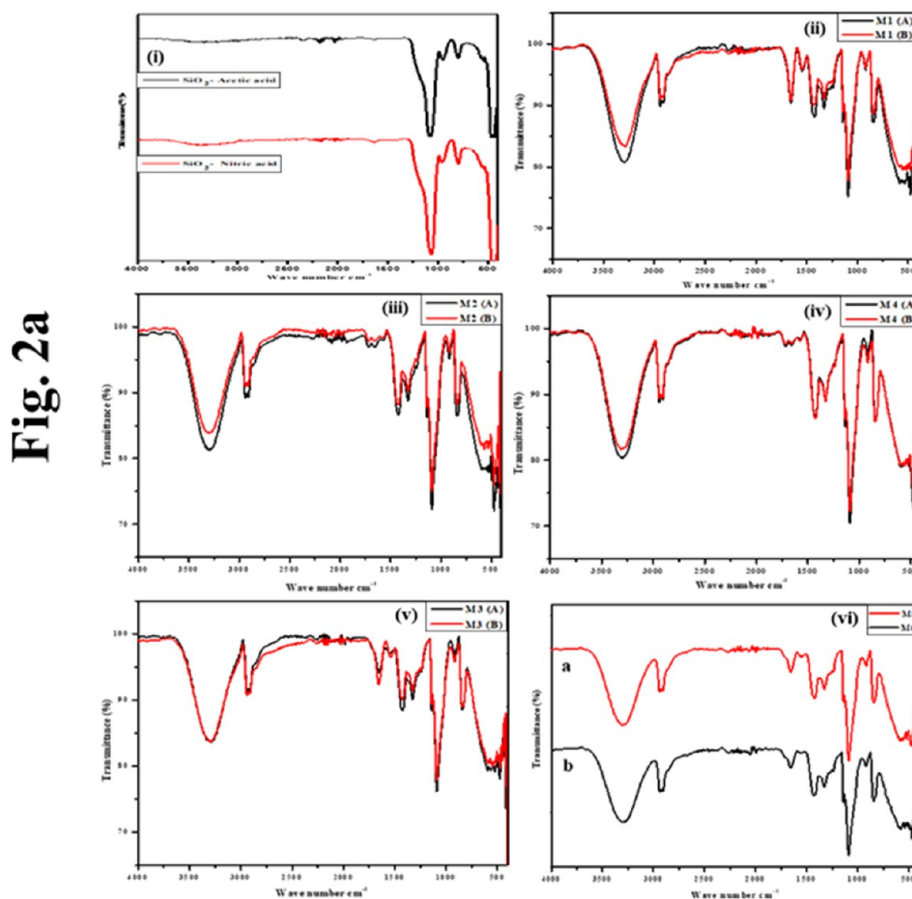
Figure 2. (a) FTIR spectra of prepared silica particles and sandwich-structured nanofibrous scaffolds (both upper and bottom layer) M1, M2, M3, and M4 and monolayered nanofibers M5 and M6. (b) Chemical bonding of prepared silica particles, silk fibroin, chitosan, and PVA.
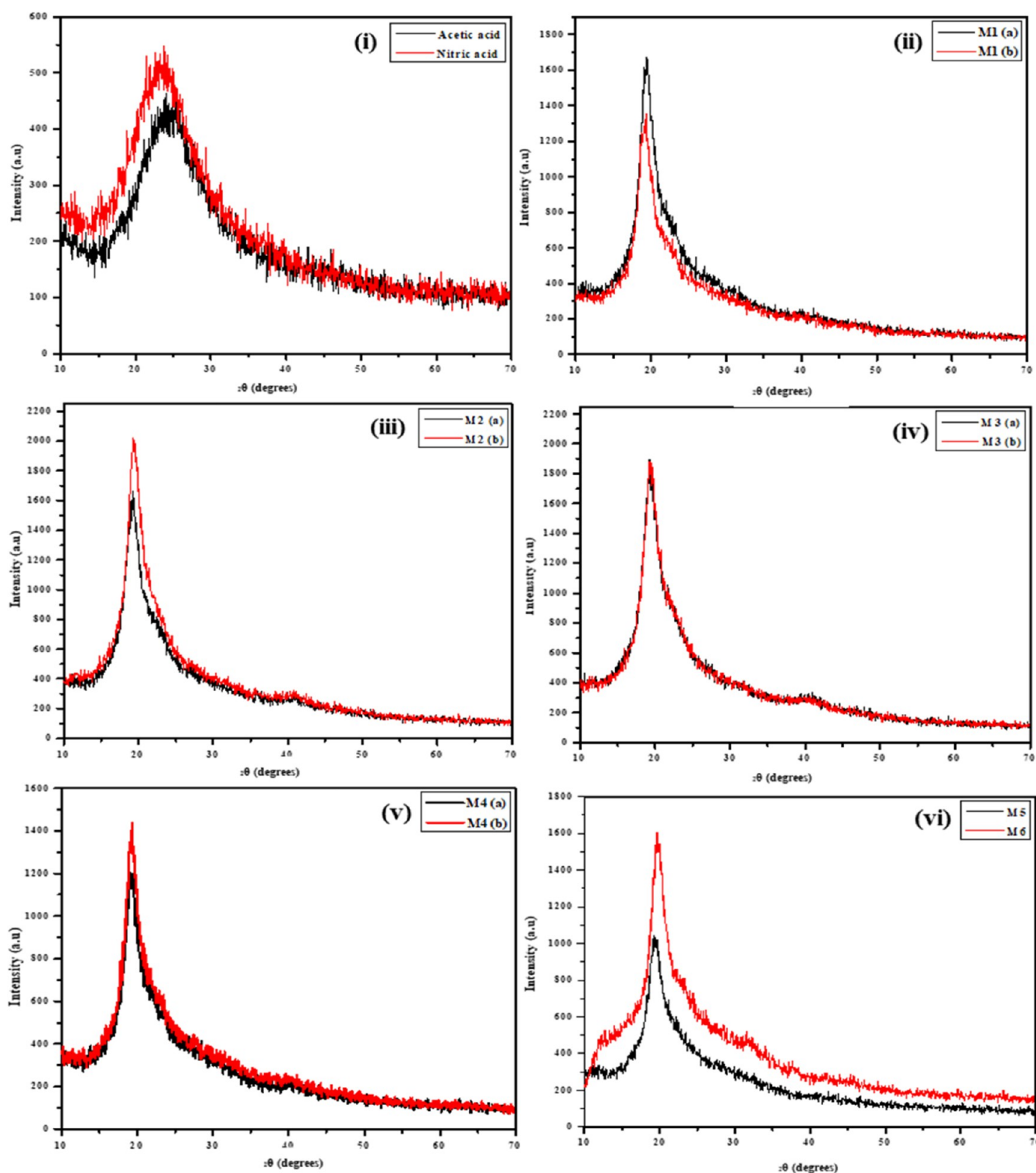
Figure 3. X-ray diffractometry graphs of prepared silica particles and sandwich-structured nanofibrous scaffolds (both upper and bottom layer) M1, M2, M3, and M4 and monolayered nanofibers M5 and M6.

siloxane (Si−O−Si) groups, and the mechanism is discussed by Brinker.[27]

In the sol−gel system, the acidity of the solution can affect the hydrolysis process of TEOS. As discussed by Vijayalakshmi and Rajeswari,[28] acidity of the solution may affect the hydrolysis and condensation process; negatively charged silica (one SiO⁻ group per 10^3 Å² of the surface) repels each other at pH 7; however, increasing the acidity of the reaction mixture

near pH ≥ 2 (i.e., relative to isoelectric point (IEP) of silica) could increase the silica network (aggregation of spherical silica particles) and decrease the particle size.[29] As a result, the diluted nitric acid could increase the gel formation rate with an increase in the porous silica network compared with acetic acid. This effect is further discussed in the XRD and FTIR analysis below. The sol−gel-derived silica particles prepared by

diluted nitric acid were then sintered at 650 °C, which was used to fabricate the designed scaffolds.

The fabricated nanofibrous scaffolds exhibit a triple-layered structure reminiscent of a "sandwich-like" orientation, comprising a middle layer enveloped by outer layers composed of the same composite (as mentioned in Table 1 and depicted in Figure 1). The electrostatic attraction occurring between the interphase regions of the same diameter thickness in the fibrous mesh increases the friction of three-dimensional scaffolds. The arrangement of the nanofibrous mesh in a sandwiched order was accomplished by varying polymer solutions A, B, and C as discussed above. The mentioned features of sandwich-structured nanofibers are successfully achieved and hold promise for fulfilling the ideal characteristics of an effective scaffold for bone regeneration.

3.2. FTIR Analysis. The functional groups of synthesized silica particles in Figure 2a(i) and (ii, iii, iv, v, vi(a,b)) show the FTIR spectra of sandwich-structured nanofibers M1, M2, M3, M4, M5, and M6, respectively. In the spectrum of Figure 2a(ii−v), red-black color curves are plotted to indicate the front and back sides of the fabricated sandwich nanofibers. The red-black curves showed similar spectral orientations of M1, M2, M3, and M4, which confirms the assembly of sandwich-like nanofibers (i.e., upper-lower layers are of the same compositions). The as-synthesized silica particles by the sol−gel method in two different acids are explained in Figure 2a(i). An absorption peak in the wavenumber of 464 and 1062 cm^{-1} was observed in Figure 2a(i) and (ii, iv, v, vi(a,b)), which are attributed to Si−O−Si bending of SiO$_2$ particles. The pure as-synthesized silica (Figure 2a(i)) showed a weak peak at 2100−2360 cm^{-1}, which may be due to Si−OH stretching that further overlaps with C=O vibrations.[30] The peak intensity that corresponds to the silica group has been increased in the case of nitric acid as a catalyst when compared to acetic acid as a catalyst. This reaction with nitric acid as a catalyst further confirms the formation of a uniform silica network.

In all of the curves of Figure 2a(ii−vi(a,b)), a broad peak at 3000−3500 cm^{-1} is associated with −OH stretching in PVA or may also belong to −OH in chitosan and a peak at 2900 cm^{-1} referred to the (−CH$_2$−) asymmetric and symmetric band of PVA. A strong peak at 840 cm^{-1} was also associated with the C−H backbone of the PVA polymer.[31] The residual N-acetyl peak at 1634 cm^{-1} in Figure 2a(iv, M3) and Figure 2a(vi(b), M6) was attributed to C=O stretching vibrations of amide I in chitosan.[32] The major peak at 1640−1650 cm^{-1} in Figure 2a(ii, iv, vi(a,b)) corresponds to C=O stretching vibrations of amide I, which confirms the presence of β-sheet conformation of SF in the composite.[33] In addition, a weak peak at 1530−1540 cm^{-1} was attributed to N−H deformation or C−N stretching of amide II, which further confirms the presence of random coil conformation in SF.[34] The hydrophobic domains (Gly−Ala−Gly−Ala−Gly−Ser) of SF are organized as β sheets embedded with amorphous hydrophilic linkages that are made up of bulky amino acid groups.

The other peaks of chitosan and silk fibroin were highly dominated by the PVA polymeric peaks. Eventually, Figure 2a(ii) depicts the functional groups of PVA/SF on the M1 surface, and Figure 2a(iii) depicts the presence of PVA, SF, and chitosan groups on M3, wherein Figure 2a(ii, iv) is ascribed to the presence of PVA and silica on M2 and M4. The structure of chitosan−silk fibroin−silica−PVA is depicted in Figure 2b, resulting in more hydrogen bonding and electrostatic attraction between the layers. Hence, from FTIR spectra,

it was evidenced that the existence of a middle layer of the nanofiber could not identified. In addition to this phenomenon, both the upper and bottom layers (red and black spectral curves) attained similar peaks, which indicates the successful fabrication of sandwich-type nanofibrous scaffolds.

Figure 2b displays the chemical bonding between the composite nanofibers. SF possesses inter- and intrachain hydrogen bonding and electrostatic bonding with other constituents in the matrix, which strengthens the mechanical properties, adhesion, and stability. Chitosan/silk and silica predominantly interact via hydrogen bonding, and hydroxyl and amine groups of chitosan/silk form hydrogen bonding with the silanol group on the surface. Maleki et al. had anticipated that due to the availability of abundant functional groups of SF (i.e., dominatingly hydroxyl functionalities), silica (i.e., silanol group on the surface) could interact with SF probably by covalent bonding, hydrogen bonding, or dipole−dipole interactions.[35] The amine group of polycationic chitosan electrostatically interacts with the negatively charged surface of silanol, contributing to stabilization of the composite structure. van der Waals interactions between chitosan/silk and silica arise from fluctuations in the electronic distribution within molecules, contributing to adhesion between different phases. Budnyak et al. reported that silica and chitosan in the matrix interact via hydrogen bonding, and the amine groups may not form covalent bonds with alkoxysilane under pH conditions.[36]

Similarly, Zhang et al. reported that PVA has more hydroxyl content at the outer side of the molecules, which interacts with silanol groups via hydrogen bonding.[37] PVA and silk molecules (i.e., charged amino groups in the side chain) can entangle due to their interfacial interactions resulting in strong ionic interactions, contributing to the compatibility of polymers in the composite. Chimprasit et al. examined the docking analysis between chitosan and silk fibroin; the study depicted silk structures' fluctuating hydrogen bond interactions (1−6) and van der Waals interactions with chitosan functionalities. In detail, ammonium groups (i.e., −NH$_3^+$) and hydroxy groups on the chitosan structure interact with the oxygen atom of the carbonyl groups on silk.[38]

3.3. X-ray Diffraction Analysis. XRD crystalline structures of calcinated silica particles using two different acids are illustrated in Figure 3(i) (i.e., silica particles prepared by acetic and nitric acids, respectively); Figure 3(ii−vi) illustrates the composite nanofibers (M1, M2, M3, M4, M5, and M6, respectively). As shown in Figure 3(i), the distinct peak in the region between 2θ at 20−21° signifies the presence of crystalline silica particles[39] in the amorphous phase and also confirms the silica-rich upper and bottom layers of M2 and M4 and M5 and M6 respectively. However, in Figure 3(i), the intensity of the diffraction peaks at 20° was found to be increased due to the formation of silica particles in the nitric acid medium when compared with that in the acetic acid medium. This depicted intensity differences in both nitric and acetic acid media were also mentioned in the above FTIR result.

The characteristic peaks of PVA in the composite nanofibers were found to be at 19.5 to 20 and 38.5−40°. The broadening of the peak at 20° may be due to the presence of intramolecular hydrogen bonding of semicrystalline PVA.[40] The diffraction peak at 24.2° was attributed to the secondary structure of SF (i.e., β-sheet conformation or silk I) and 28.43° (silk II), which was found on the surface of M1, M3, M5, and
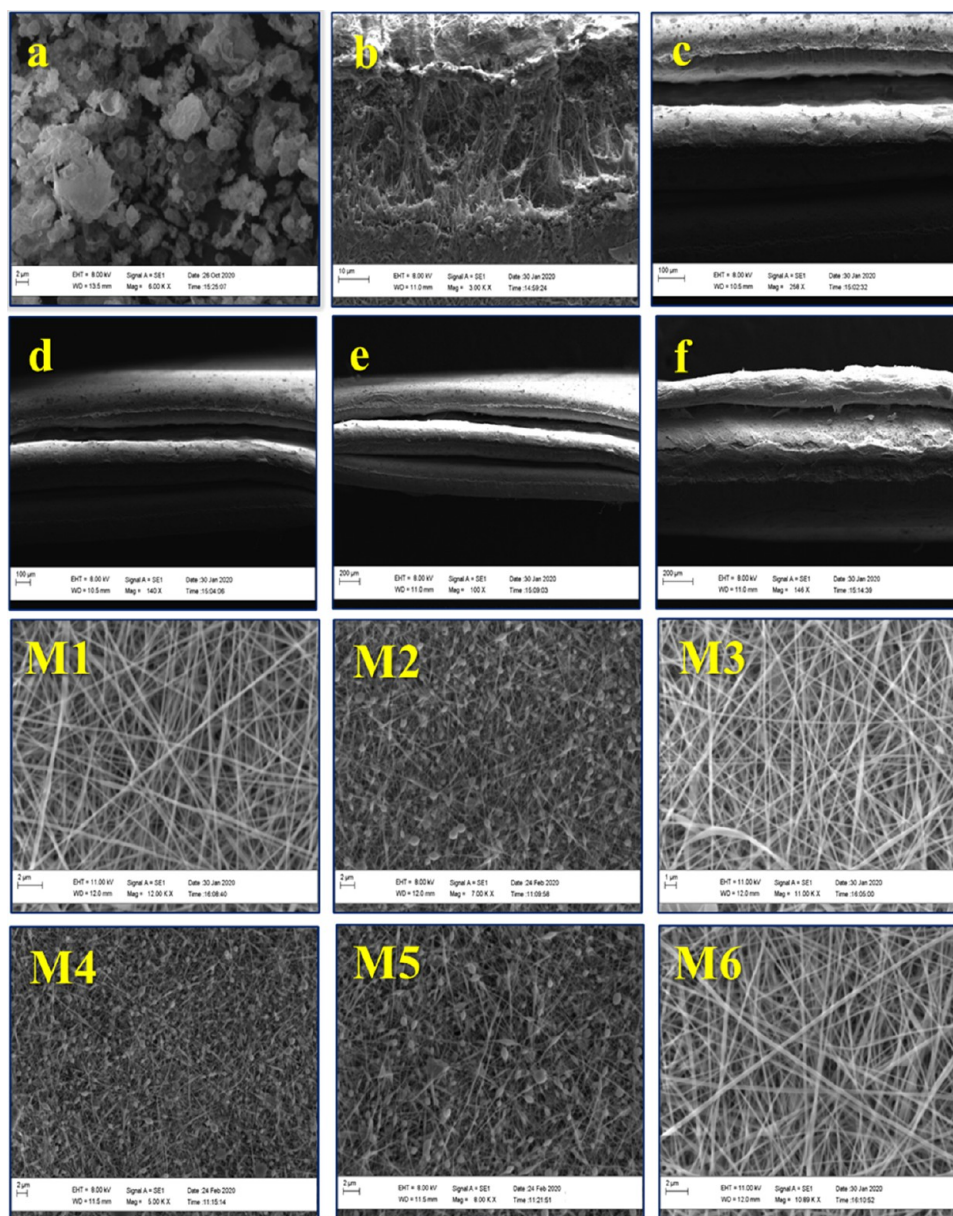
Figure 4. Micrographs of prepared silica particles (a), cross-sectional view of sandwich-layered nanofibers (b), and side view of layer-by-layer assembly of M1 (c), M2 (d), M3 (e), and M4 (f) nanofibers and surface morphology of sandwich-structured nanofibrous scaffolds M1, M2, M3, and M4 and monolayered nanofibers M5 and M6.

M6 scaffolds, respectively.[41] Major peaks at 14.5 and 20.1° were identified for the hydrated crystalline structure of chitosan in the M3 and M6 nanofibrous mesh.[42] In addition, the upper surface (curves) and the bottom surface (*b* curves) of the nanofibers resulted in a similar XRD pattern, which confirms the orientation of sandwich-type scaffolds as discussed in FTIR analysis. Taken together, the intensity peak increased and was found to be more in M3 than M6, which is associated with the presence of chitosan.

3.4. Membrane Morphology. SEM micrographs in Figure 4a show the spherical-like silica nanoparticles prepared by the sol−gel method using nitric acid as a catalyst, and Figure 4b shows the cross-sectional view of sandwich-layered nanofibers in a different composition of PVA/silica/SF/CS. The cross-sectional view showed that the fiber connections of three distinct layers produced by the electrospinning process created a thick microstructural layer. Figure 4c−f shows a side

view of the layer-by-layer assembly of M1, M2, M3, and M4 nanofibers in a randomly orientated manner. Figure 4(M1, M3) shows the microstructural morphology with average diameter, which indicates the bead-free fabrication of SF/PVA composite nanofibers, and there are no silica particles on the surface.

Padaki et al. reported that the morphology and the diameter of the nanofibers depend upon many parameters such as polymer concentration, viscosity, nature and type of the polymer, composition of the spinning solution, applied voltage, flow rate, and solution conductivity.[43] The micrograph of Figure 4(M2, M4) shows a uniform distribution of the silica particle microbeads embedded in the PVA mesh, and Figure 4(M5, M6) demonstrates the nanofiber surface with the composition of PVA/silica/SF and PVA/silica/SF/chitosan monolayers. Furthermore, the fiber diameter of the nanofibers was measured using SEM images, and the calculated fiber
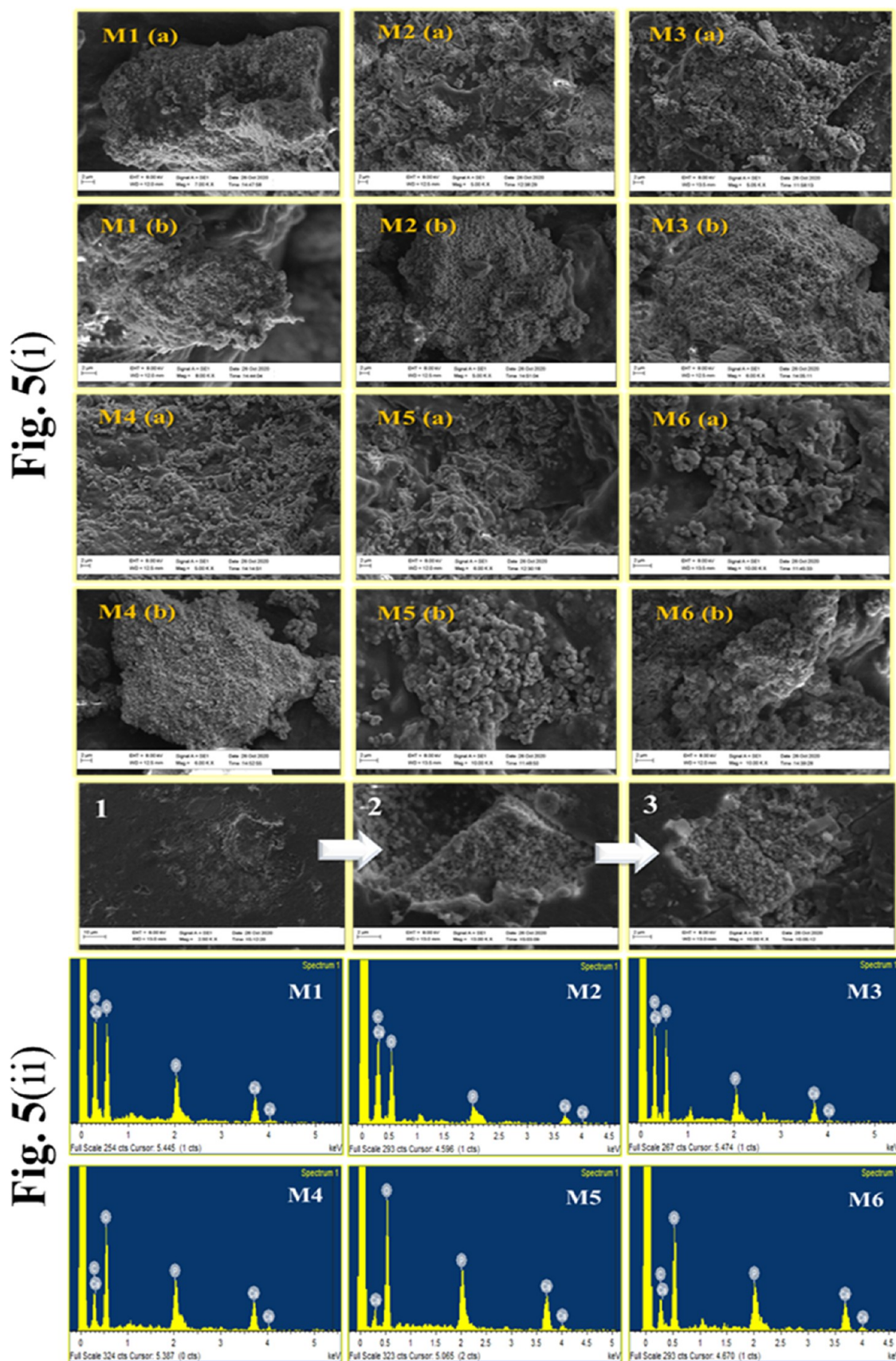
Figure 5. (i) Micrographs of a spherical-like apatite on the surface of sandwich-structured and monolayered scaffolds. (i) (1, 2, 3) Mechanism of the biomineralization process on sandwich scaffolds. (ii) EDAX spectrum of biomineralized sandwich-structured and monolayered scaffolds after 14 days of immersion in the SBF solution.
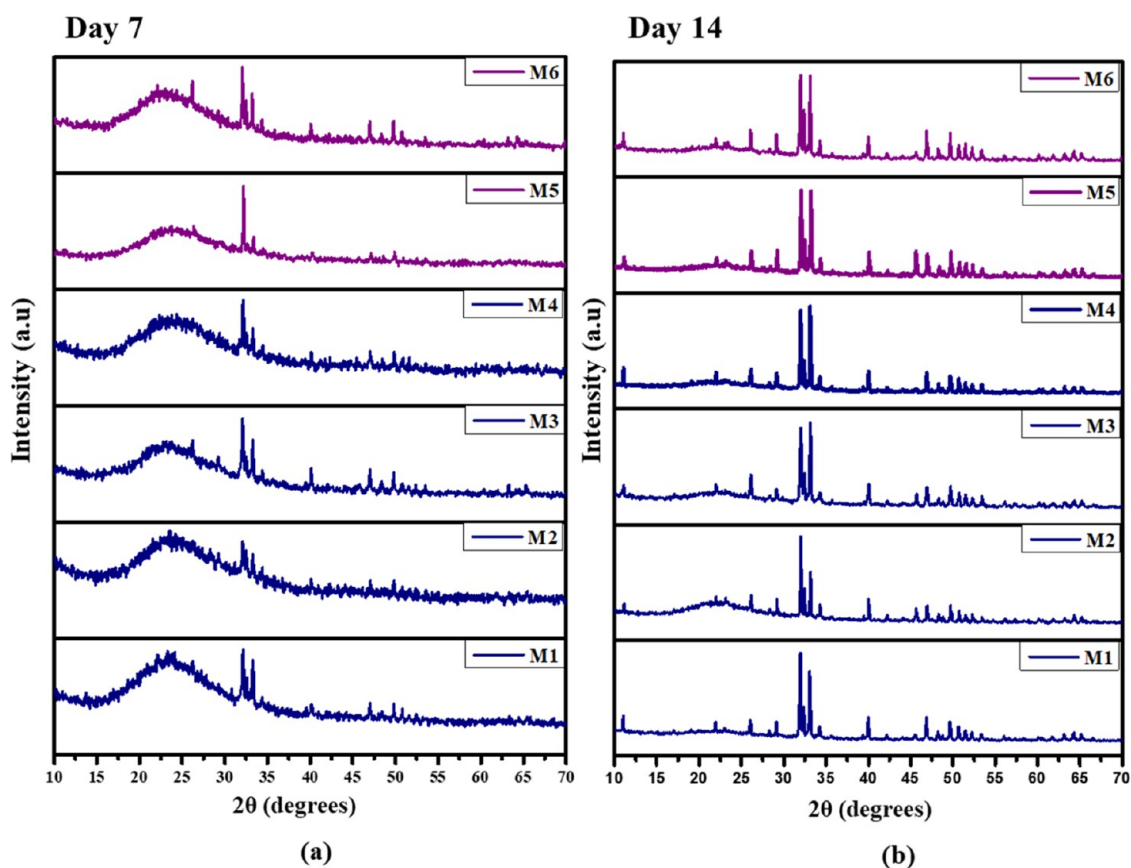
Figure 6. (a, b) XRD spectrum of biomineralized sandwich-structured and monolayered scaffolds after 7 and 14 days of SBF immersion.

diameter of M1, M2, M3, M4, M5, and M6 ranged from ∼100 ± 9.9 to 250 ± 13.2 nm (Figure S1, Supporting Information File). The fiber diameter increased significantly with the inclusion of silk and chitosan in the composite nanofibers. Zhao et al. observed that the incorporation of chitosan and silk fibroin increased the diameter.[44] The inclusion of silica particles increased the viscosity of the spinning solution, causing a slight increase in the fiber diameter, as observed on the surface of the M2, M4, M5, and M6 scaffolds. The inclusion of silica particles can act as a nucleation site for phase separation or polymer crystallization, leading to a finer nanofiber structure and confirming the polymer chain during fiber formation. Malczewska et al. reported that the inclusion of silica particles in the spinning solution decreases the fiber diameter, however enhanced the antibacterial and mechanical properties.[45] The top views of all of the nanofibers were randomly aligned on each layer, which is in accordance with FTIR and XRD graphs.

3.5. In Vitro Biomineralization of the Sandwiched and Monolayered Scaffolds. *3.5.1. SEM.* The apatite deposition on the scaffolds is closely related to osteogenic differentiation in vivo; Figure 5(i) illustrates the biomineralized sandwich-type nanofibers incubated at 7 and 14 days in SBF to examine the formation of an apatite layer on the scaffold. The appearance of a spherical-like apatite layer was confirmed by scanning electron microscopy (SEM) and was further investigated by XRD and FTIR analyses. Microstructure apatite was formed on the surface of M1, M2, M3, M4, M5, and M6 composite nanofibers when the scaffolds were immersed in an SBF solution of 37 °C for 7 and 14 days. The presence of free ions in SBF with the surface of the

scaffolds makes them interact together, which leads to a biomineralization process (i.e., nucleation of apatite followed by a growth process). Besides, the scaffolds exhibited that spherical HCA (hydroxy carbonated apatite) particles dispersed more uniformly on the nanofiber mesh after biomineralization. The occurrence of dense spherical-like apatite particles was found to be larger in number on the surfaces of M1 and M3. This may be due to the increased porous microstructure in the presence of SF and SF/chitosan, which could act as a base for bone ingrowth. In addition, M2 and M4 have also resulted in dense apatite formation (i.e., silica-rich surface may react with metastable ions in the SBF solution) but comparatively less than M1 and M3. The ion exchange or dissolution−precipitation mechanism between free ions of the SBF solution with the Si−O⁻···H⁺-rich surface of M2 and M4 scaffolds (i.e., degradation of the silanol group (Si−O−H) from the silica network) could induce the apatite formation. According to Takadama et al.,[46] calcium (Ca^{2+}) free ions in the SBF solution can chelate with negatively dissociated silanol radicals (i.e., Si−O⁻ degradation from the composite during SBF immersion) to form unstable amorphous calcium silicate (Si−O−Ca⁺). Subsequently, these positively charged calcium radicals bind with negatively charged phosphate ions in SBF immersion, leading to apatite formation (amorphous calcium phosphate). For sandwich-layered nanofibers, dynamic biomineralization occurs by surface dissolution of M2 and M4 (where Si/PVA is the outer layer), and complete dissolution of M1 and M3 nanofibers (where Si/PVA is the middle layer) in prolonged SBF immersion leads to the precipitations of a dense apatite layer on the surface.
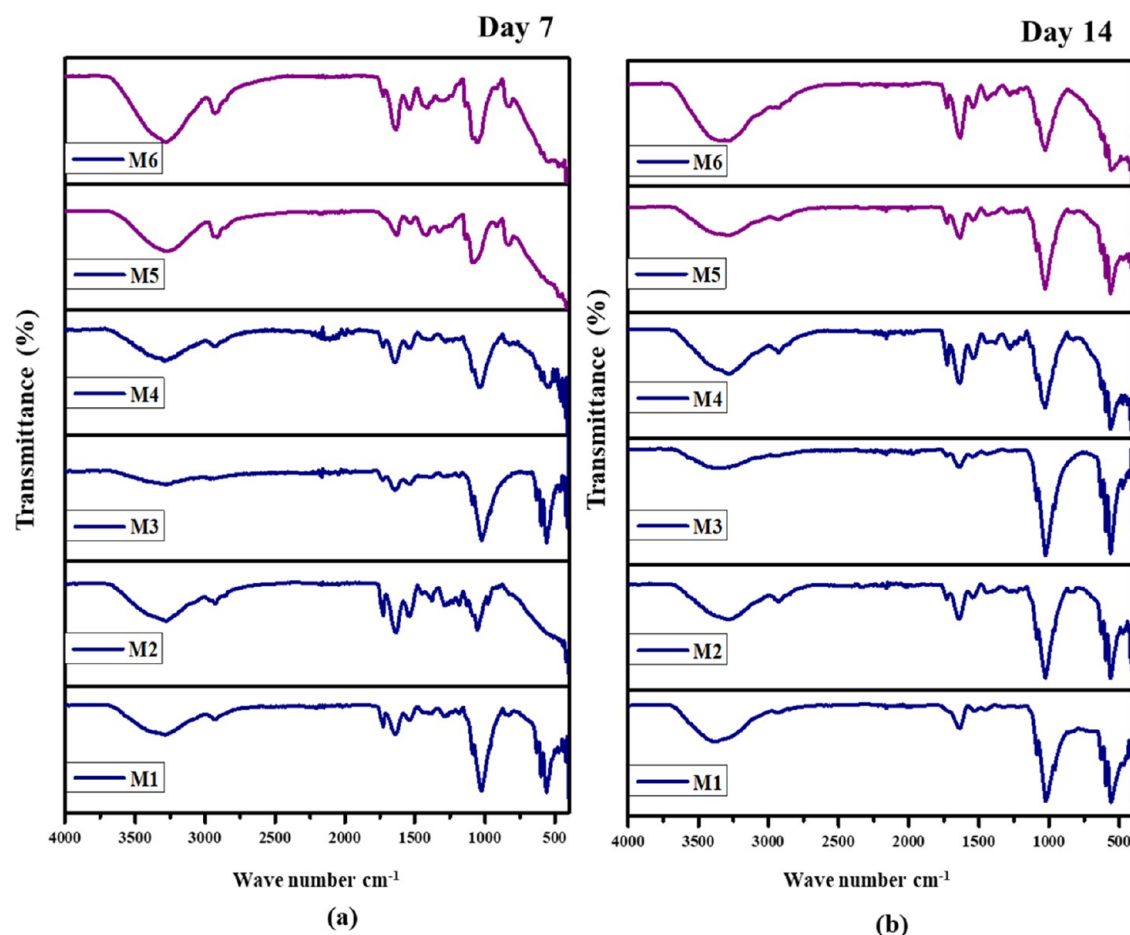
Figure 7. (a, b) FTIR spectra of biomineralized sandwich-structured and monolayered scaffolds after 7 and 14 days of SBF immersion.

The higher densification of apatite particles (i.e., deposition of carbonated calcium phosphate layer) was seen on the 14th day with complete apatite coverage (coating) on the porous nanofibrous network. In addition, the combinatory interactions of SF with chitosan on the M3 upper layer increased the level of in vitro calcium phosphate deposition more than M4. Figure 5((i)(1,2,3)) represents the SEM micrograph of the biomineralized surface on the nanofibrous scaffold after SBF immersion for the duration of 14 h. The transformations of the surface from the nanofibrous scaffold to the seeding of the apatite layer are completely visible in the figure. Hence, the coverage of the apatite layer is confirmed by the biomineralization process.

3.5.2. EDAX Analysis. The elemental analysis of biomineralized scaffolds after 14 days of immersion is shown in Figure 5(ii). The Ca/P ratios of M1, M2, M3, M4, M5, and M6 of 14 day immersed samples are 1.83, 1.77, 1.81, 1.78, 1.89, and 1.82, respectively. From the ratio, it was clear that all sandwich layers had shown a higher Ca/P ratio (i.e., Ca/P > 1.67, stoichiometric ratio of hydroxyapatite) due to the formation of HCA. The presence of SF increased the biomineralization process, thereby increasing the percentage of Ca and P content, and no other Si was seen on the surface after the biomineralization process. Noteworthily, the elemental analysis of EDAX graphs proved the complete biomineralization process on the surface of the scaffolds.

3.5.3. XRD and FTIR of Biomineralized Scaffolds. The formation of apatite on the SBF-immersed scaffold for 7 and 14 days was further analyzed by FTIR and XRD analyses. The prolonged immersion of the scaffold increased the dense layer formation of amorphous hydroxyl carbonated apatite on the surface, where the addition of SF also increased the nucleation process. Analysis of spectra in Figure 6a,b illustrates the XRD pattern, and Figure 7a,b illustrates the FTIR pattern of the scaffold after 7 and 14 days of immersion. As shown in Figure 4(a,b), comparatively, M1, M3, M5, and M6 scaffolds have shown a major peak intensity in the 2θ range at 31.74° (which coincides with the crystal phase JCPDS no. 09-0432 of HAP) than M2 and M4 scaffolds.[47] In addition, the high-intensity peak at around 31−32° exhibited in all of the samples may correspond to the biomineralized calcium apatite structure in SBF immersion. The diffraction peak in the range of 20° was found to be broader on day 7 and became weak after day 14. Relatively, on increasing the immersion period from 7 to 14 days, the observed calcium apatite peak appeared with high intensity, where the silica and polymer peak became weakened. Hence, the XRD data of day 14 also confirmed the presence of a dense apatite layer with greater degrees of crystallinity on all of the scaffold surfaces. The sharp diffraction peak at the plane (002) indicated the existence of an amorphous bone-like carbonated apatite on the surface, which is compatible with SEM data.

FTIR spectra (Figure 7a,b) showed a broad vibrational band at around 3200−3300 cm^{-1}, which originated due to the presence of hydrogen bonding (O−H− stretching) of absorbed water molecules. The asymmetrical stretching and
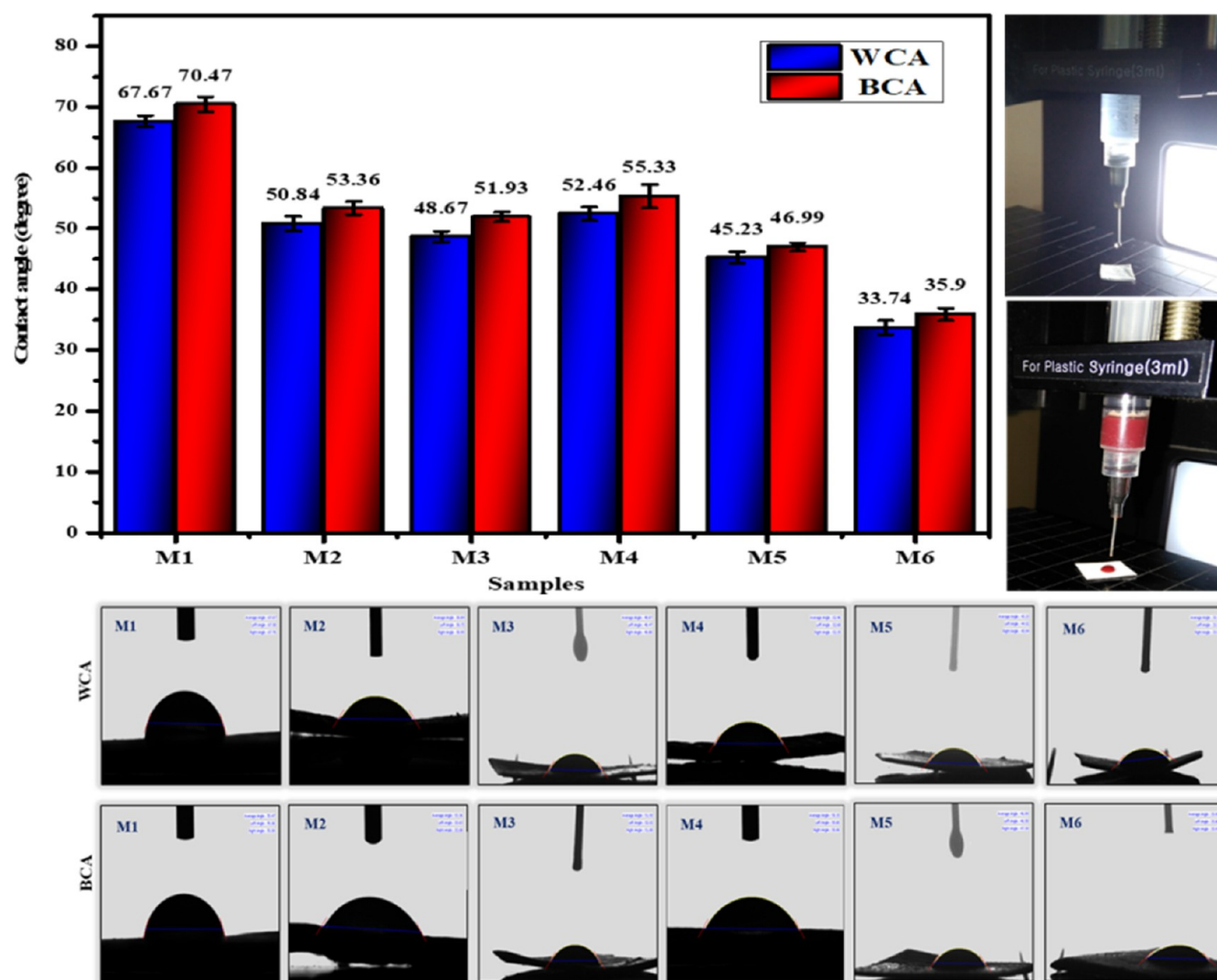
Figure 8. Water contact angle (WCA) and blood (BCA) wettability of sandwich-structured and monolayered scaffolds.

bending modes of phosphate ions (PO_4^{3-}) were detected at around 605 and 1034 cm^{-1} ($\nu 1$) and a triplet band at 465−554 cm^{-1} ($\nu 4$) in all of the immersed scaffolds for 7 and 14 days. Meanwhile, the carbonated stretching (i.e., deposition of carbonated apatite layer) is found at 838 and 1416−1420 cm^{-1} ($\nu 3$), which confirms the formation of type B carbonated apatite ions.[48,49] From the biomineralization results, a strong indication of bone-like apatite formation (HCA) proved an increase in peak intensities with an increase in the immersion period.

XRD and FTIR peaks depict the dense formation of carbonated HAP (hydroxyapatite) nanogranules on the surface of all scaffolds and were found more in sandwich-type multilayered scaffolds. The more carbonated apatite peaks were obtained on the SF-embedded scaffold (M1, M3, M5 and M5) surface, which may be due to the presence of amine and carbonyl groups belonging to SF. These groups can absorb Ca^{2+} ions in the metastable SBF solution and later chemically bond with PO_4^{3-} and OH$^-$ ions in an antithetical way to induce a biomineralization process.[50,51] The presence of silanol groups (Si−OH−) on the interfacial sandwich-like layers of M2 and M4 and monolayered M5 and M6 can chelate the calcium ions in the SBF solution to form a cluster-like

amorphous calcium apatite.[52] This cluster could regulate the spontaneous nucleation on the composite nanofibers as SF regulates. Though the sandwich layer scaffolds (M1, M2, M3 and M4) have delaminated layers (also discussed in the mechanical study), the apatite growth was increased with the increase of soaking time.

3.6. Wettability of the Water Contact Angle (WCA) and Blood Contact Angle (BCA). The wettability of monolayered and sandwich-layered nanofibers was characterized by contact angle measurements, as shown in Figure 8. The high hydrophilic surface was observed on monolayered nanofibers compared to multilayered nanofibrous scaffolds. This affinity for water may be due to the thickness of the fibers and the respective composites on the surface of the nanofibers. On comparing all scaffolds, the multilayer sandwich-type M3 scaffold has been shown to be more hydrophilic than M1, whereas M2 and M4 have shown similar values. The high affinity is manifested in the SF/CS/PVA surface layer of M3 compared to that in the SF/PVA surface layer of M1. The observed hydrophilicity may be due to the hydrophilic nature of CS and the hydrophobic nature of SF. SF contains a stable β-sheet conformation that shows less hydrophilicity when compared to CS.[53,54] The contact angles of M2 and M4
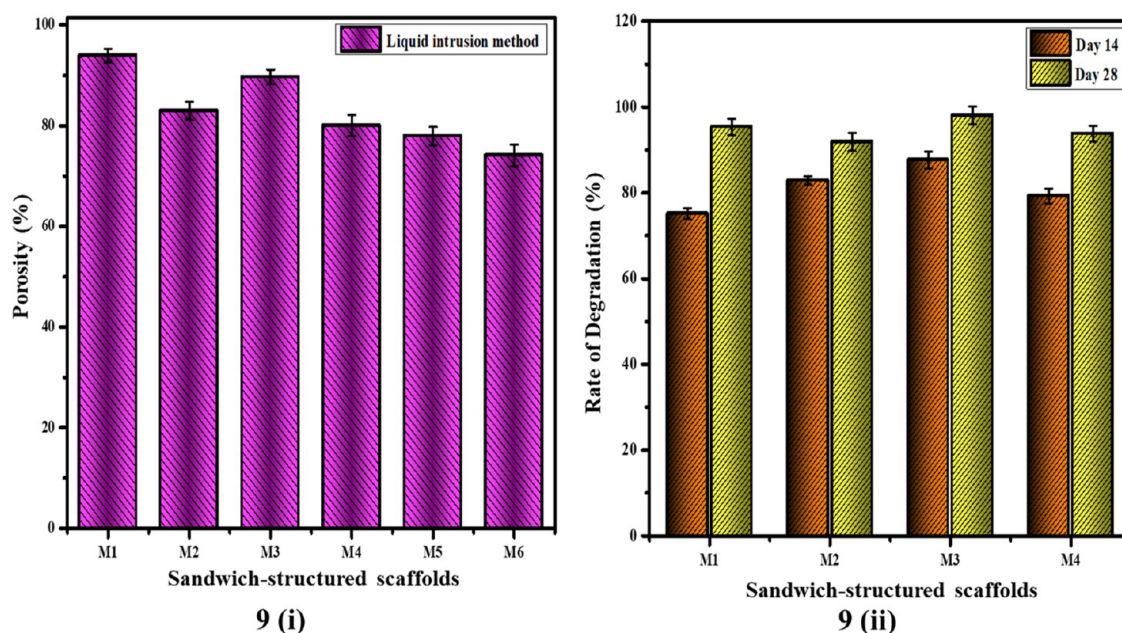
Figure 9. (i) Porosity measurement of sandwich-structured and monolayered scaffolds using the liquid intrusion method. (ii). Degradation profile of sandwich-structured and monolayered scaffolds.

exhibited similar hydrophilic effects (i.e., Si/PVA) with approximately similar values. Although silk fibroin (M1 nanofiber) has more hydrophilic groups such as −CH and −COOH, silica (M2 and M4 nanofibers) resulted in higher water/blood hydrophilicity due to the hydrogen bonding in the silanol group and also may be due to the formation of spatial net structures formed via a Si−O−Si linkage,[55] as proved in the FTIR result. It is a well-known fact that surface energy increases the interaction between the biological environment (i.e., cell attachment), and the surface of the scaffold is prime important for biological activity.

3.7. Porosity Measurement and In Vitro Biodegradation Profile. Porosity and degradation properties are essential for transporting oxygen and nutrients throughout the scaffolds, and they have additional important effects on cell migration and proliferation, where porosity can still facilitate the degradation rate. Figure 9(i) shows the degradation properties in an SBF solution at different soaking times, and the porosity of sandwich-type scaffolds was evaluated using the liquid intrusion method. As shown in Figure 9(i), the weight loss of scaffolds displays an increasing tendency with the presence of silk fibroin and chitosan content. Specifically, the average porosities of the scaffolds M1, M2, M3, M4, M5, and M6 at the incubation period of 48 h are 93 ± 1.34, 82.98 ± 1.76, 89.71 ± 1.45, 80.05 ± 2.10, 77.97 ± 1.80, and 74.11 ± 2.16, respectively. The scaffolds with more SF concentration have better porosity than silica in the nanofibers, which could also be reasonable for cumulative cell proliferation.[56] The chitosan can decrease the porosity of the nanofibers until it is functionalized with other groups.[57] The silica-incorporated fibers as the covering layer in M2 and M4 showed better porosity, which was less than M1 and M3 (i.e., SF on the surface). As a result, the porosity of all fibers remains >80% except M5 and M6.

Moreover, the degradation profile (Figure 9(ii)) of sandwich scaffolds (M1, M2, M3, M4) for 14 and 28 days of SBF immersion are 75.12 ± 1.32, 82.89 ± 0.98, 87.67 ± 2.02, and 79.24 ± 1.69 and 95.34 ± 1.91, 91.88 ± 2.11, 98.07 ± 2.08,

and 93.76 ± 1.87, respectively. Sandwich scaffolds exhibited slower and steady biodegradation compared to the monolayered scaffolds, which is due to the thickness of the fibers. Therefore, on comparing only the sandwich type, there was an increase in the rate of degradation with respect to prolonged incubation (i.e., 14 to 28 days), and after attaining its saturation stage, the degradation rate decreased, so the deformation occurred. The continual degradation of the scaffolds reached up to 90% in chitosan scaffolds (M3), wherein the presence of acetyl units has more chance to degrade them.[58] From the degradation study, it was observed that the scaffolds with higher degradation rates are the ones with higher porosity; thereby, it could promote higher cell viability effectively during in vivo or further in vitro studies.

3.8. Mechanical Evaluation of Sandwich-Type Nanofibers. Mechanical strength was performed for a monolayer (M5, M6) and sandwich-layered nanofibrous mats (M1, M2, M3, M4) under static conditions using a universal testing machine (Figure 10). Mechanical testing may depend on nanofiber diameters, alignment, effects of fiber conglutination, and entanglements inside nanofibrous mats.[59] All of the fibrous sandwich mats were fabricated with similar diameters (i.e., the thickness of the nanofibers), as shown in Figure 10a, along with delamination picturization. Tensile strength and stress at break were calculated from the stress−strain response of the tested samples. Sandwich-layered nanofibers (M1, M2, M3, M4) have shown excellent tensile strength compared with monolayer nanofibers (M5, M6). From the experimental observation, the delamination of sandwich-layered nanofibers (i.e., when the stress increases, the sandwich-type fibers undergo delamination of individual layers that deform plastically) was evidenced, as shown in Figure 10. Additionally, it was observed that M2 showed the highest strength (10.73 MPa) than M4 (9.21 MPa). The tensile strength of nanofibers increases in the presence of a silica particle-embedded PVA matrix. Silica particles act as a stress concentrator by increasing the stiffness of the matrix system.[60] Hence, the scaffold with
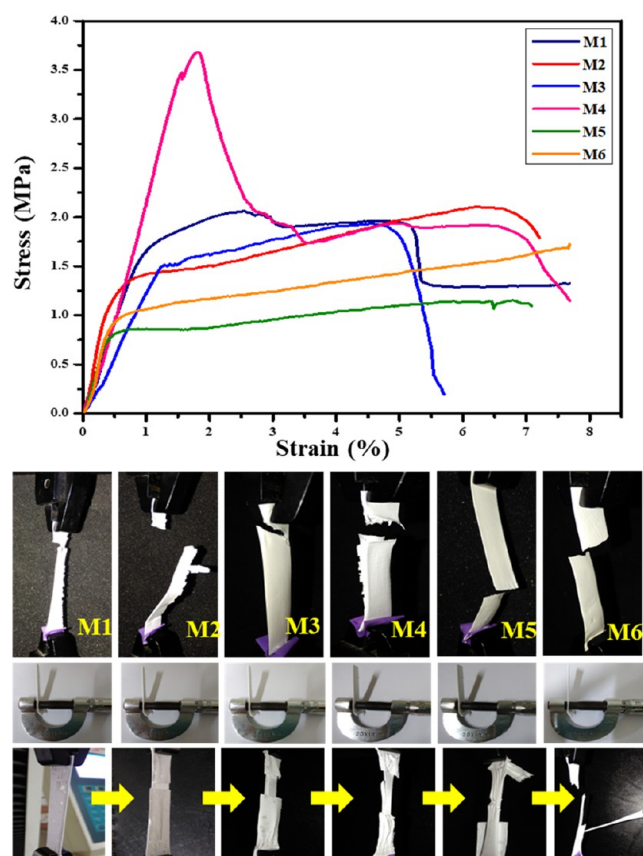
Figure 10. Mechanical evaluation: stress−strain graph of sandwich-structured and monolayered scaffolds and delamination versus thickness photographs of sandwich scaffolds. (Photograph courtesy of "Author: R.M." Copyright 2024).

Figure 11. Hemolytic analysis of sandwich-structured and monolayered scaffolds. The (*) represents that the difference is statistically significant at $p < 0.01$ (data represent the mean $\pm$ standard deviation of M1, M2, M3, M4, M5 and M6).

$PVA + SiO_2$ as the outer layer exhibited more strength than scaffolds with $PVA + SF/PVA + SF + CS$ as the outer layer.

Though M1 and M3 have less silica, M1 showed higher strength than M3 due to SF concentration. The presence of β-sheet crystallites in SF forms strong van der Waals hydrogen bonding that leads to hydrophobic interaction, which may increase the stiffness and toughness of the nanofibers.[61] Additionally, chitosan in M3 and M6 nanofibers can monotonically decrease the tensile strength by increasing the brittleness.[62,63] Among all of the scaffolds, M4 has more strength where the outer layer is comprised of $PVA + SiO_2$ and the inner layer is comprised of $PVA + SF + CS$. So, both SF and CS in the polymeric network lead to additional benefits to the scaffold, where the outer layer with SiO_2 combination gives better results for the study.

3.9. Hemolytic Assay. The interaction of biomedical devices with blood platelets after implantation can cause undesirable consequences or activation of coagulation under a biophysical environment. The degree of mutual adaptation (hemocompatibility of the scaffolds) can be assessed by performing in vitro hemolytic assay according to the ISO 10993-4 standard. Figure 11 shows the OD values and microscopic images of the hemolysis test of the sandwich-type nanofibrous membranes. The positive reference is 100% hemolytic, and the corresponding negative reference is 0%. The hemolysis of M1, M2, M3, M4, M5, and M6 was observed as 1.09 ± 0.018, 1.17 ± 0.026, 1.11 ± 0.029, 1.15 ± 0.035, 1.07 ± 0.023, and 1.05 ± 0.041, respectively. The obtained values

are significantly lower than the positive control group (data represent the mean $\pm$ standard deviation of M1, M2, M3, M4, M5 and M6 (1.87×10^{-8}, which is $p < 0.01$)). Dehghani et al. reported that the biodegradation of chitosan in the human body could induce hemostasis by inhibiting fibrinolysis during the hemostatic phase; however, these lysozyme byproducts are harmless and metabolized. In detail, the positively charged chitosan groups react with negatively charged platelets and erythrocytes, leading to aggregation (i.e., hemostasis), whereas functional groups of chitosan such as hydroxyl carboxyl and amino groups undergo chemical modification.[64] All of the scaffolds exhibited a hemolysis value of less than 5%. It further indicates that the fabricated nanofibrous composite samples are blood-compatible. Moreover, the microscopic images of red blood cells are not ruptured in shape when treated with test samples after incubation.

3.10. Antibacterial Activity. Figure 12 shows the antibacterial results of nanofibers and their ability to inhibit the growth of *S. aureus* and *E. coli*. The inhibitory activity was relatively lower toward *E. coli* than the inhibitory activity toward *S. aureus*, and this cause may be due to the compositions of Gram-positive and negative bacterial cell walls. It was noted that the inhibitory activity of M6 nanofibers was increased when compared to M5. However, on account of sandwich-type nanofibers, M3 showed higher activity than M4, M2, and M1. This is probably attributed to the outer layer of chitosan with silk fibroin in PVA, and the bactericidal effect may be influenced by the combinational effect of chitosan, silk fibroin, and silica in the scaffold. The presence of hydroxyl (−OH) radical groups in the chitosan produces an exerting
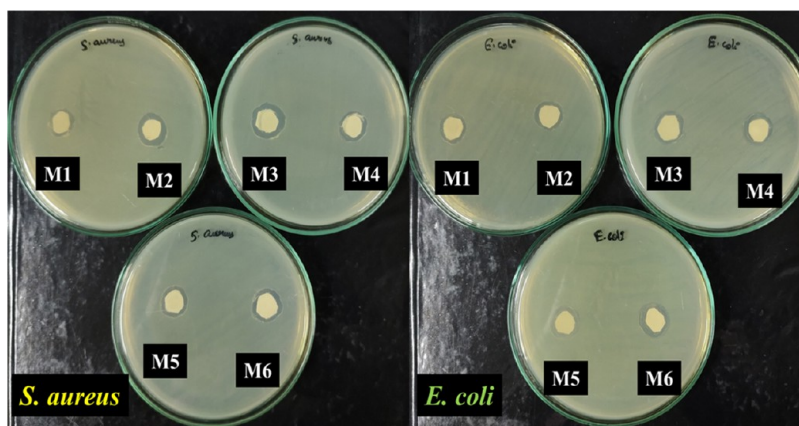
Figure 12. Antibacterial assay of sandwich-structured and monolayered scaffolds. (Photograph courtesy of "Author: R.M." Copyright 2024).

oxidative stress-rich surface charge density and binds with negatively charged bacterial cell walls (such as nucleic acid and proteins), later destroying DNA bacteria (i.e., chitosan can increase the antibacterial effect against *E. coli*).[65] Souto-Lopes et al. reported that chitosan could interact with the peptidoglycan layer of Gram-positive bacteria and disturb the cell functions, whereas the interaction with Gram-negative bacteria interrupts the membrane integrity and inhibits DNA/RNA synthesis of bacteria.[66] The study suggested that chitosan in the nanofibrous composite (i.e., M3 and M6) can induce oxidative stress against bacteria that could prevent bacterial adhesion compared with other compositions (i.e., M1, M2, M4 and M5). Both M6 and M3, having the composition of CS + SiO_2 + PVA, exhibited excellent antibacterial effects in both *S. aureus* and *E. coli*, respectively. Further, the M5 scaffold, which has the composition of SF + SiO_2 + PVA, also exhibits a good antibacterial effect. Hence, the presence of chitosan in the scaffolds reveals more effect than the other scaffolds.

3.11. Cell Proliferation on the Scaffold Using the MG63 Cell Line. The MG63 (human osteoblast-like) cell line was seeded into the prepared nanofibrous scaffold, and it was kept under the culture period for 1 to 7 days. As shown in Figure 13, the cell attachment and proliferation were performed on sandwich-type nanofibers. The results showed significant statistical differences in the cell proliferation of composite nanofibers (M1 ($p = 0.0061$), M2 ($p = 0.0071$), M3 ($p = 0.0051$), M4 ($p = 0.0073$), M5 ($p = 0.0040$), M6 ($p = 0.0035$)) at 24, 48, and 72 h of incubation (i.e., overall p-value <0.05). Perceptively, with an increase in the incubation period, there is a gradual increase in the cell viability of the MG63 cell line due to the degradation of the nanofiber during the incubation period. After 168 h of incubation, M1 and M3 showed higher proliferation at 87.03 ± 0.37 and 98.64 ± 0.28, respectively. The scaffolds, such as M2 and M4, have shown the same cell viability as the surface is shielded with Si/PVA as a covering layer. M1 and M3 are sandwich-structured scaffolds bearing SF/CS/PVA on the covering surface where all three components are hydrophilic. As discussed in Section 3.7, the rate of cell proliferation gradually increased due to the increase in the degradation rate and porosity with prolonged incubation.[67,68] In particular, MG63 cell viability of M1 agrees with our previous findings that SF could promote cell viability by creating pores in the surface via degradation (i.e., cells grew on the porous surface).[20]

The cell viability of all of the composite sandwich-layered and monolayered nanofibers showed no toxic effect on the
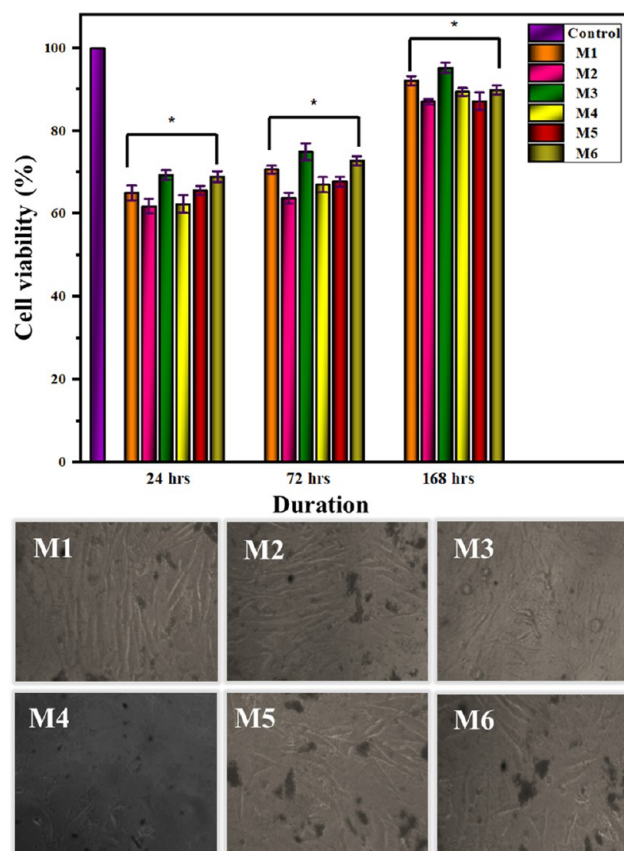
Figure 13. MTT assay using the MG63 cell line of sandwich-structured and monolayered scaffolds for 1, 3, and 7 days and microscopic images of MG63 cells on the scaffolds at day 7. The (*) displays the difference is statistically significant at $p < 0.05$ (data represent the mean ± standard deviation of M1, M2, M3, M4, M5 and M6).

MG63 cell line, indicating all of the scaffolds are biocompatible. In addition, the cell adhesion increased due to the hydrophilic nature of the prepared nanofibers, and the presence of the outer covering layer also demonstrated the cell viability. Moreover, the electrostatic interaction of chitosan with phospholipids in cell membranes, hydrogen bonding, as well as hydrophobic interactions of the silk fibroin β sheet could impart cell adhesion and proliferation.[69] The combinations of dual fibrous protein in the composite could increase
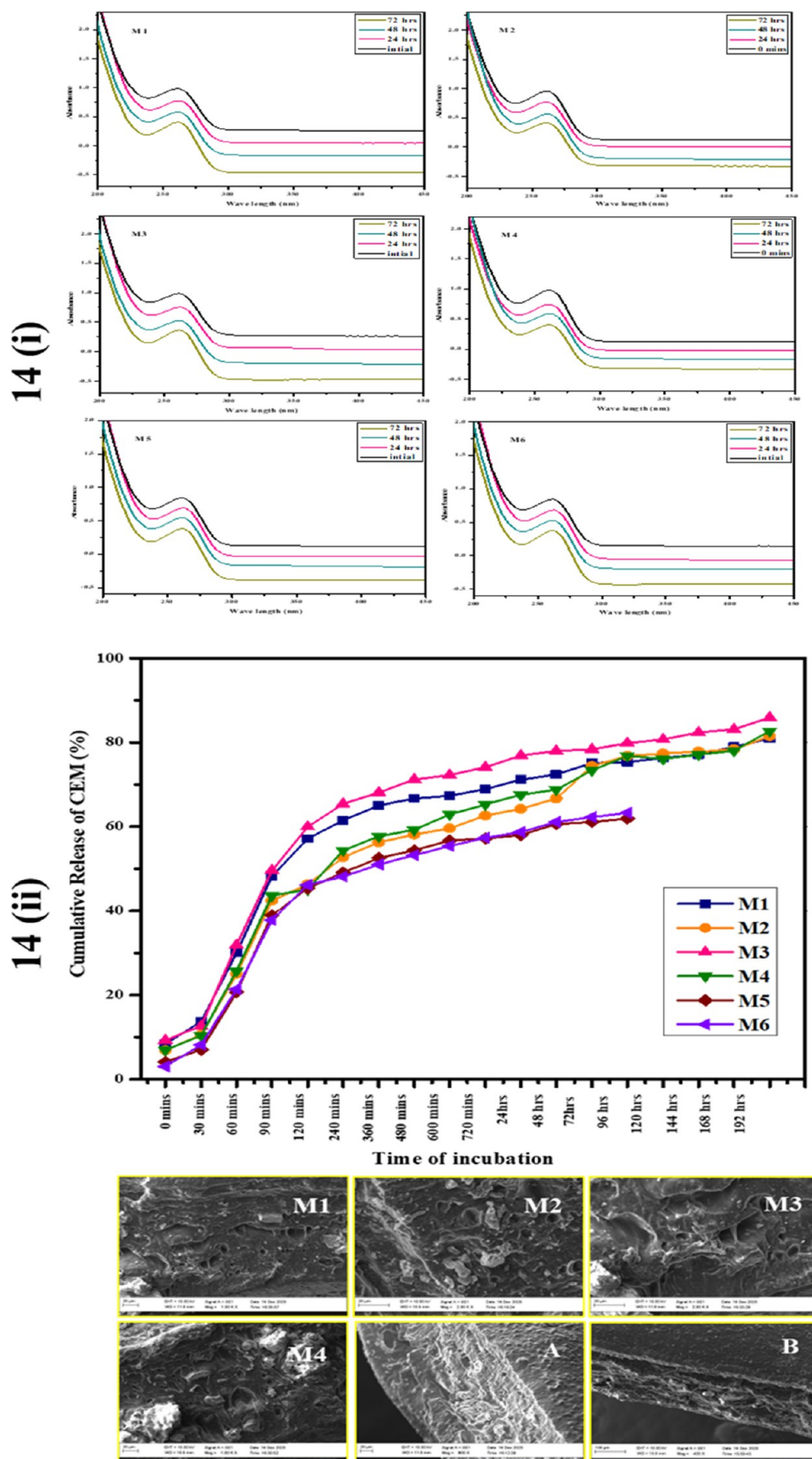
Figure 14. (i) UV spectrum of CEM loading profiles sandwich-structured and monolayered scaffolds. (ii) Cumulative drug release profile from CEM-loaded sandwich-structured and monolayered scaffolds.

the cell proliferation rate and also enhance the molecular functions of signaling molecules at the active site, thereby regulating cellular pathways, which is in accordance with our previous findings.[70] In detail, biopolymers can accelerate angiogenesis and promote better cell proliferation by forming physicochemical interactions and a better scaffold surface and cell membrane via ionic forces during regeneration. The synergistic effect of chitosan and silk fibroin had a higher cellular affinity toward the MG63 cell line, which could promote cell proliferation, thus making the composite a potential candidate for bone tissue engineering.

3.12. In Vitro Drug Delivery of Scaffolds. 3.12.1. Drug-Loading Profile.
The CEM drug is the most prevailing β-lactam antibiotic agent against bacterial infections that includes the gastrointestinal tract, soft tissue, urinary tract, eye, bone, skin, ear, respiratory tract, etc. In our previous finding, we reported the mechanism of the CEM drug, interfering with the bacterial cell wall, causing a rupture and annihilating the bacteria.[71] The drug delivery property of the sandwich-like layered scaffolds was evaluated using the CEM drug. Figure 14i represents the loading efficiency of the nanofibers measured by UV−visible spectroscopy. The absorption peak at 260 nm was observed for all of the drug-loaded nanofibrous scaffolds. The percentage of loading efficiency was found to be 59.17 ± 2.23, 55.88 ± 2.35, 63.43 ± 2.11, 56.67 ± 1.99, 47.84 ± 2.09, and 49.26 ± 2.41 for M1, M2, M3, M4, M5, and M6 respectively. The loading percentage of CEM was found to be higher in sandwiched nanofibers, whereas, in the case of single-layered nanofibers, it was found to be less. Also, electrospun nanofibers gained more attention as drug carriers due to their flexibility and large surface area to diffuse drugs at the targeted site.[72] This fact indicated that M1, M2, M3, and M4 layered nanofibers (∼30 mm diameter thickness) are more porous on the surface (where the upper layer and middle layer of the same composite are super hydrophilic as well). A natural polymer such as silk fibroin and chitosan in the polymeric matrices has a swelling ratio higher than silica in PVA, thereby it impacts in the release of drugs.[73] The swelling of drug molecules by a natural polymer dissolves or diffuses and creates electrostatic/ionic interactions or hydrophilic interactions with the hydrophobic group in the natural polymer (dominatingly β-sheet conformation of silk fibroin), resulting in an expansion mechanism.[74] This swelling nature increases porosity (literally voids) to elute drug molecules from the matrix system (here, scaffold) in a PBS medium, hence modulating degradation more easily with a prolonged release of the residence time. The hydrophobic interaction of amino acid groups of silk fibroin and chitosan provides the encapsulation of CEM in an aqueous medium and drug-loading permeability.

If the drug is delivered or released quickly, there may be a chance of infection due to the release of the entire drug from the scaffold; if the drug is released very slowly, there may be a chance of difficulty in wound healing properties. Hence, the slow release of the drug is very important for effective use in medical applications. Studies have shown that silica is capable of entrapping an 8-fold greater quantity of drug species than calcium phosphate.[75] The delayed release profile is possible with silica nanofibers; in the present study, CEM has been loaded successfully and done in an effective way to release the drug in different periods.

3.12.2. Drug Releasing Profile.
The cumulative release of antibiotic CEM and SEM images after drug release in PBS is shown in Figure 14(ii), where the cumulative amount of the drug released was calculated before the release percentage from the scaffolds. Sandwich-structured scaffolds showed immediate burst release for 120 min followed by prolonged release for up to 192 h in an aqueous medium. This prolonged release might be related to the hydrophilic groups on the surface of the nanofibers and also may be due to the electrostatic interaction between hydroxyl groups of SF/chitosan with silicate groups embedded in PVA matrices (i.e., sandwich-like orientation). As mentioned, the maximum release was found in M3 scaffolds as it was covered by a natural polymer (SF/CS) and consisted of the center layer as silicates. The higher porosity, which might be due to the presence of silk fibroin, could increase fluid absorption and aid sustained release in long-term applications.[76] This is further evidenced by the SEM images of M1, M2, M3, and M4, as shown in Figure 14(ii), where pores were obtained after the complete release of CEM from scaffolds.

The cationic nature of primary amino groups of chitosan can deliver micro- and nanoparticles due to its pH sensitivity, mucoadhesivity, biodegradability, and other chemical features. As proof of concept, Vivek et al. anticipated that a change in pH from 4.5 to 7.5 of chitosan decreased the drug release, and a higher surface area of chitosan increased the drug release.[77] Recently, Hasanbegloo et al. reported that paclitaxel drug release was found to be more from liposome-incorporated chitosan-based nanofibers due to a weak carboxyl group of chitosan and more swelling at pH 5.5.[78]

The side view of the sandwich-structured scaffolds (Figure 14((ii)(A,B)), after complete release) retained trilayered alignment with pores, which is also taken as evidence for the prolonged release that occurred due to the electrostatic attraction between hydrophilic adhesive layers.[79] Besides, the middle layer covered by the composite (Si/PVA, M1 and M3) or PVA/SF/CS (M4) or Si/PVA/SF/CS (monolayered M5 and M6) showed initial burst release (and later reduced), followed by prolonged release due to the covering layer (i.e., where covalent bond interactions would take place between the drug with composite molecules). At 192 h, almost all of the drug was released from the scaffolds via degradation/erosion of the polymeric matrix by the so-called monolithic drug delivery.[80] In a physiochemical environment, the drug-loaded matrix may undergo diffusion and swelling, which create pores, followed by erosion or degradation of the system.[81]

Delan et al. suggested that drug-loaded PVA nanofibers in pH 7 could undergo hydration (absorb water), swell, and change the physiochemical properties of the composite nanofibers, which further enables drug release via erosion or matrix relaxation.[82] Typically, natural polymer-based drug delivery systems are intended to have two stages of delivery, such as drug diffusion, followed by biodegradation of the drug delivery system (i.e., scaffold). All of the scaffolds showed sustained release behavior for longer periods except M5 and M6, where it continued only up to 96 h. The release behavior of CEM from scaffolds was correlated to first-order kinetics, where the polymer followed a slow diffusion rate in the medium.

4. CONCLUSIONS

In this study, we designed a trilayered sandwich-like" organic/inorganic hybrid scaffold using an electrospinning technique. The following conclusions have been drawn from the above findings.

- The cross-sectional view of SEM analysis confirmed the existence of a designed trilayered sandwich-like nanofibrous network.

- From the in vitro biomineralization process, the formation of dense spherical-like particles was observed on M3 (PVA/SF/CS as outer layers) and M1(PVA/SF as outer layers) compared with other scaffolds. This was further confirmed by FTIR and XRD with the reduction of the silica peak by the increase in the apatite peak at around $31°(2\theta)$.

- The higher porosity might be due to the well-ordered sandwich-like layers with its associated interconnected pores. Moreover, the presence of a hydrophilic nature and higher degradation of the M3 scaffold (i.e., SF/CS outer layers) can further promote the cell proliferation effect in biocompatibility assessment using the MG63 cell line. Antibacterial inhabitance and hemocompatibility assessment were confirmed for the developed scaffolds.

- Among all of the scaffolds, M3(PVA/SF/CS as outer layers) and M1 (PVA/SF as outer layers) showed less stiffness with adequate mechanical strength, which helps in the degradation of CEM at prolonged duration. The mechanical stability of sandwich-like scaffolds was 3 times stronger than monolayered scaffolds.

- From the findings, the hydrolyzed silica with silk fibroin/chitosan interconnected network ($-Si-O-Si-SF/Cs$) increased the electrostatic interactions between the layered mesh, thereby enhancing the biological property.

- Consequently, the imperative stiffness coupled with sustained drug release from the customized sandwich-like scaffolds could effectively inhibit bacterial infection and enhance bone regeneration.

ASSOCIATED CONTENT

SI Supporting Information

The Supporting Information is available free of charge at https://pubs.acs.org/doi/10.1021/acsomega.4c01069.

Average diameter evaluated by its microstructural morphology (the nanofiber consisting of PVA/silica/SF/CS showed that the fiber connections of three distinct layers were produced by the electrospinning process. A layer-by-layer assembly of M1, M2, M3, and M4 nanofibers indicates the fabrication of composite nanofibers without defect-free. The fiber diameter increased significantly with the inclusion of silk and chitosan in the composite nanofibers) (Figure S1) (PDF)

AUTHOR INFORMATION

Corresponding Author

Vijayalakshmi Uthirapathy − *Department of Chemistry, Vellore Institute of Technology, Vellore 632 014, India;* orcid.org/0000-0003-0727-4277;
Email: vijayalakshmi.u@vit.ac.in, lakesminat@yahoo.com

Authors

Rama Murugapandian − *Centre for Nonlinear Systems, Chennai Institute of Technology, Chennai 600069, India*

Sundara Ganeasan Mohan − *Department of Analytical Chemistry, University of Madras, Chennai 600025, India*

Sridhar T M − *Department of Analytical Chemistry, University of Madras, Chennai 600025, India*

N. Arunai Nambi Raj − *Centre for Biomaterials, Cellular and Molecular Theragnostic, Vellore Institute of Technology, Vellore 632 014, India*

Complete contact information is available at:
https://pubs.acs.org/10.1021/acsomega.4c01069

Notes

The authors declare no competing financial interest.

REFERENCES

(1) Sun, Y.; Li, R.; Yu, X.; Li, X.; Han, Z.; Sun, J.; Bi, W.; Liu, W.; Yu, Y.; Cui, W. Highly active biological dermal acellular tissue scaffold composite with human bone powder for bone regeneration. *Mater. Des.* **2021**, *209*, No. 109963.

(2) Zhao, C.; Shu, C.; Yu, J.; Zhu, Y. Metal-organic frameworks functionalized biomaterials for promoting bone repair. *Mater. Today Bio* **2023**, *21*, No. 100717.

(3) Matsubara, T.; Yamada, K.; Kanazawa, T.; Sato, K.; Yokosuka, K.; Shiba, N. Improved intervertebral bone union in ALIF rat model with porous hydroxyapatite/collagen combined with platelet-rich plasma. *Spine J.* **2023**, *23*, 325−335.

(4) He, Y.; Wang, W.; Lin, S.; Yang, Y.; Song, L.; Jing, Y.; Zhang, Z. Y.; et al. Fabrication of a bio-instructive scaffold conferred with a favorable microenvironment allowing for superior implant osseointegration and accelerated in situ vascularized bone regeneration via type H vessel formation. *Bioact. Mater.* **2022**, *9*, 491−507.

(5) Boyetey, M.-J. B.; Torgbo, S.; Sukyai, P. Bio-scaffold for bone tissue engineering with focus on bacterial cellulose, biological materials for hydroxyapatite synthesis and growth factors. *Eur. Polym. J.* **2023**, *194*, No. 112168.

(6) Moghadam, E. T.; Yazdanian, M.; Alam, M.; Tebyanian, H.; Tafazoli, A.; Tahmasebi, E.; Ranjbar, R.; Yazdanian, A.; Seifalian, A. Current natural bioactive materials in bone and tooth regeneration in dentistry: a comprehensive overview. *J. Mater. Res. Technol.* **2021**, *13*, 2078−2114.

(7) Mombini, S.; Mohammadnejad, J.; Bakhshandeh, B.; Narmani, A.; Nourmohammadi, J.; Vahdat, S.; Zirak, S. Chitosan-PVA-CNT nanofibers as electrically conductive scaffolds for cardiovascular tissue engineering. *Int. J. Biol. Macromol.* **2019**, *140*, 278−287.

(8) Szymańska-Chargot, M.; Chylińska, M.; Pertile, G.; Pieczywek, P. M.; Cieślak, K. J.; Zdunek, A.; Frąc, M. Influence of chitosan addition on the mechanical and antibacterial properties of carrot cellulose nanofibre film. *Cellulose* **2019**, *26*, 9613−9629.

(9) Haider, A.; Haider, S.; Kummara, M. R.; Kummara, M. R.; Kamal, T.; Alghyamah, A. A. A.; Iftikhar, F. J.; Iftikhar, F. J.; Bano, B.; Khan, N.; Afridi, M. A.; Han, S. S.; Alrahlah, A.; Khan, R. Advances in the scaffolds fabrication techniques using biocompatible polymers and their biomedical application: A technical and statistical review. *J. Saudi Chem. Soc.* **2020**, *24*, 186−215.

(10) Wang, Z.; Wang, Y.; Yan, J.; Zhang, K.; Lin, F.; Xiang, L.; Deng, L.; Guan, Z.; Cui, W.; Zhang, H. Pharmaceutical electrospinning and 3D printing scaffold design for bone regeneration. *Adv. Drug Delivery Rev.* **2021**, *174*, 504−534.

(11) Xing, J.; Zhang, M.; Liu, X.; Wang, C.; Xu, N.; Xing, D. Multi-material electrospinning: from methods to biomedical applications. *Mater. Today Bio* **2023**, *21*, No. 100710.

(12) Dejob, L.; Toury, B.; Tadier, S.; Gremillard, L.; Gaillard, C.; Salles, V. Electrospinning of in situ synthesized silica-based and calcium phosphate bioceramics for applications in bone tissue engineering: A review. *Acta Biomater.* **2021**, *123*, 123−153.

(13) Martín-Moldes, Z.; Ebrahimi, D.; Plowright, R.; Dinjaski, N.; Perry, C. C.; Buehler, M. J.; Kaplan, D. L. Intracellular pathways involved in bone regeneration triggered by recombinant silk−silica chimeras. *Adv. Funct. Mater.* **2018**, *28*, No. 1702570.

(14) Zhang, P.; Chen, J.; Sun, Y.; Cao, Z.; Zhang, Y.; Mo, Q.; Yao, Q.; Zhang, W. A 3D multifunctional bi-layer scaffold to regulate stem cell behaviors and promote osteochondral regeneration. *J. Mater. Chem. B* **2023**, *11*, 1240−1261.

(15) Rama, M.; Suresh, A. S.; Vijaylal, L.; John, A. E.; Vijayalakshmi, U. A Review on Nanofibrous Scaffolding Technique for Potential Tissue Engineering Applications. *Trends Biomater. Artif. Organs* **2022**, *36* (1), 27−37.

(16) Wang, C.; Xu, J.; Ke, S.; Li, Y.; Zhu, X.; Gu, X.; Kan, C.; Shi, D. Silver nanowires deposited on cellulose nanofibers/graphene oxide hybrid membranes as sandwich-structured films for optoelectronic and SERS applications. *ACS Appl. Nano Mater.* **2020**, *3* (11), 10844−10854.

(17) Yahia, S.; Khalil, I. A.; El-Sherbiny, I. M. Sandwich-like nanofibrous scaffolds for bone tissue regeneration. *ACS Appl. Mater. Interfaces* **2019**, *11* (32), 28610−28620.

(18) Wang, J.; Shao, L.; Wu, X.; Liu, C.; Ni, S.; Dai, T.; Liu, H.; Zhao, H. Electrospun sandwich mesh structures loaded with naringenin and vitamin K2 polycaprolactone/gelatin nanofibers synergistically promote bone regeneration. *Mater. Today Bio* **2023**, *23*, No. 100794.

(19) Rama, M.; Vijayalakshmi, U. Synergism of silver/CEM drug on novel proteinaceous silk fibroin/mesoporous silica based sandwich-layered nanofibrous scaffolds for osteoregenerative applications. *Ceram. Int.* **2023**, *49*, 17032−17051.

(20) Rama, M.; Vijayalakshmi, U. Influence of silk fibroin on the preparation of nanofibrous scaffolds for the effective use in osteoregenerative applications. *J. Drug Delivery Sci. Technol.* **2021**, *61*, No. 102182.

(21) Kokubo, T.; Takadama, H. How useful is SBF in predicting in vivo bone bioactivity? *Biomaterials* **2006**, *27*, 2907−2915.

(22) Abdelaziz, D.; Hefnawy, A.; Al-Wakeel, E.; El-Fallal, A.; El-Sherbiny, I. M. New biodegradable nanoparticles-in-nanofibers based membranes for guided periodontal tissue and bone regeneration with enhanced antibacterial activity. *J. Adv. Res.* **2021**, *28*, 51−62.

(23) Nokoorani, Y. D.; Shamloo, A.; Bahadoran, M.; Moravvej, H. Fabrication and characterization of scaffolds containing different amounts of allantoin for skin tissue engineering. *Sci. Rep.* **2021**, *11*, No. 16164.

(24) Samadian, H.; Farzamfar, S.; Vaez, A.; Ehterami, A.; Bit, A.; Alam, M.; Goodarzi, A.; Darya, G.; Salehi, M. A tailored polylactic acid/polycaprolactone biodegradable and bioactive 3D porous scaffold containing gelatin nanofibers and Taurine for bone regeneration. *Sci. Rep.* **2020**, *10*, No. 13366.

(25) Priyadarshini, B.; Rama, M.; Latha, S.; Vijayalakshmi, U. Fabrication of Zirconia by Co-Precipitation Method; Their Structural Phase Effects, Mechanical and Biological Evaluation for Biomedical Application. *Trends Biomater. Artif. Organs* **2021**, *35* (2), 161−167.

(26) Kumar, P.; Kumar, S.; Sagar, M. K. Formulation and evaluation of sustained release matirx tablet of vildagliptin using natural and synthetic polymers. *Int. J. Adv. Sci. Technol.* **2019**, *28*, 1649−1663.

(27) Brinker, C. J. Hydrolysis and condensation of silicates: effects on structure. *J. Non-Cryst. Solids* **1988**, *100*, 31−50.

(28) Vijayalakshmi, U.; Rajeswari, S. Development of silica glass coatings on 316L SS and evaluation of its corrosion resistance behavior in Ringer's solution. *Metall. Mater. Trans. A* **2012**, *43*, 4907−4919.

(29) Chou, K. T.; Lee, B. I. Properties of silica gels prepared from high-acid hydrolysis of tetraethoxysilane. *Ceram. Int.* **1993**, *19*, 315−325.

(30) Zhao, Z.; Cui, Y.; Kong, Y.; Ren, J.; Jiang, X.; Yan, W.; Li, M.; Tang, J.; Liu, X.; Shen, X. Thermal and mechanical performances of the superflexible, hydrophobic, silica-based aerogel for thermal insulation at ultralow temperature. *ACS Appl. Mater. Interfaces* **2021**, *13*, 21286−21298.

(31) Alwan, T. J.; Toma, Z. A.; Kudhier, M. A.; Ziadan, K. M. Z. Preparation and characterization of the PVA nanofibers produced by electrospinning. *Madridge J. Nanotechnol. Nanosci.* **2016**, *1*, 1−3.

(32) Lungu, R.; Anisiei, A.; Rosca, I.; Sandu, A. I.; Ailincai, D.; Marin, L. Double functionalization of chitosan based nanofibers towards biomaterials for wound healing. *React. Funct. Polym.* **2021**, *167*, No. 105028.

(33) Kuang, D.; Yu, W.; Liu, J.; Yin, Y.; Wang, C. Flexible MWCNT/Silk fibroin film decorated with Pt NPs for electrochemical glucose sensors. *Microchem. J.* **2023**, *191*, No. 108760.

(34) Xue, S. H.; Xie, H.; Ping, H.; Li, Q. C.; Su, B. L.; Fu, Z. Y. Induced transformation of amorphous silica to cristobalite on bacterial surfaces. *RSC Adv.* **2015**, *5*, 71844−71848.

(35) Maleki, H.; Shahbazi, M. A.; Montes, S.; Hosseini, S. H.; Eskandari, M. R.; Zaunschirm, S.; Verwanger, T.; Mathur, S.; Milow, B.; Krammer, B.; Hüsing, N. Mechanically strong silica-silk fibroin bioaerogel: a hybrid scaffold with ordered honeycomb micro-morphology and multiscale porosity for bone regeneration. *ACS Appl. Mater. Interfaces* **2019**, *11* (19), 17256−17269.

(36) Budnyak, T. M.; Pylypchuk, I. V.; Tertykh, V. A.; Yanovska, E. S.; Kolodynska, D. Synthesis and adsorption properties of chitosan-silica nanocomposite prepared by sol-gel method. *Nanoscale Res. Lett.* **2015**, *10* (1), No. 87.

(37) Zhang, Y.; Liu, Z.; Cao, Y.; Li, R.; Jing, Y. Impact of binder composition on inkjet printing paper. *BioResources* **2015**, *10*, 1462−1476, DOI: 10.15376/biores.10.1.1462-1476.

(38) Chimprasit, A.; Hannongbua, S.; Saparpakorn, P. Adsorption study of lac dyes with chitosan coated on silk fibroin using molecular dynamics simulations. *J. Mol. Graphics Modell.* **2021**, *106*, No. 107934.

(39) Abdeali, G.; Farhang, Z.; Bahramian, A. R. Enhancing paraffin wax crystallization and investigating thermo-physical properties of ethylene-propylene-diene monomer/paraffin wax/silica phase change system: The influence of silica nanoparticles. *J. Energy Storage* **2024**, *76*, No. 109795.

(40) Arthanari, S.; Mani, G.; Jang, J. H.; Choi, J. O.; Cho, Y. H.; Lee, J. H.; Cha, S. E.; Oh, H. S.; Kwon, D. H.; Jang, H. T. Preparation and characterization of gatifloxacin-loaded alginate/poly (vinyl alcohol) electrospun nanofibers. *Artif. Cells, Nanomed., Biotechnol.* **2016**, *44*, 847−852.

(41) Yang, F.; Wang, F.; Mazarreh, J.; Hu, X. Ultrasound-assisted air-jet spinning of silk fibroin-soy protein nanofiber composite biomaterials. *Ultrason. Sonochem.* **2023**, *94*, No. 106341.

(42) Qiao, C.; Ma, X.; Zhang, J.; Yao, J. Effect of hydration on water state, glass transition dynamics and crystalline structure in chitosan films. *Carbohydr. Polym.* **2019**, *206*, 602−608.

(43) Padaki, M.; Subramanya, T. M.; Prasad, D.; Déon, S.; Jadhav, A. H. Electrospun nanofibers: role of nanofibers in water remediation and effect of experimental variables on their nano topography and application processes. *Environ. Sci.: Water Res. Technol.* **2021**, *7*, 2166−2205.

(44) Zhao, W.; Cao, S.; Cai, H.; Wu, Y.; Pan, Q.; Lin, H.; Fang, J.; He, Y.; Deng, H.; Liu, Z. Chitosan/silk fibroin biomimic scaffolds reinforced by cellulose acetate nanofibers for smooth muscle tissue engineering. *Carbohydr. Polym.* **2022**, *298*, No. 120056.

(45) Malczewska, B.; Lochyński, P.; Charazińska, S.; Sikora, A.; Farnood, R. Electrospun Silica-Polyacrylonitrile Nanohybrids for Water Treatments. *Membranes* **2023**, *13* (1), No. 72.

(46) Takadama, H.; Kim, H. M.; Kokubo, T.; Nakamura, T. Mechanism of biomineralization of apatite on a sodium silicate glass: TEM− EDX study in vitro. *Chem. Mater.* **2001**, *13*, 1108−1113.

(47) Wang, S.; Yang, Y.; Wang, R.; Kong, X.; Wang, X. Mineralization of calcium phosphate controlled by biomimetic self-assembled peptide monolayers via surface electrostatic potentials. *Bioact. Mater.* **2020**, *5*, 387−397.

(48) Jaramillo-Martínez, S.; Vargas-Requena, C.; Rodríguez-Gónzalez, C.; Hernández-Santoyo, A.; Olivas-Armendáriz, I. Effect of extrapallial protein of Mytilus californianus on the process of in vitro biomineralization of chitosan scaffolds. *Heliyon* **2018**, *5*, No. e02252, DOI: 10.1016/j.heliyon.2019.e02252.

(49) Dal Sasso, G.; Asscher, Y.; Angelini, I.; Nodari, L.; Artioli, G. A universal curve of apatite crystallinity for the assessment of bone integrity and preservation. *Sci. Rep.* **2018**, *8*, No. 12025.

(50) Gao, Y.; Shao, W.; Qian, W.; He, J.; Zhou, Y.; Qi, K.; Wang, L.; Cui, S.; Wang, R. Biomineralized poly (l-lactic-co-glycolic acid)-tussah silk fibroin nanofiber fabric with hierarchical architecture as a scaffold for bone tissue engineering. *Mater. Sci. Eng.: C* **2018**, *84*, 195−207.

(51) Xiao, L.; Wu, M.; Yan, F.; Xie, Y.; Liu, Z.; Huang, H.; Yang, Z.; Yao, S.; Cai, L. A radial 3D polycaprolactone nanofiber scaffold modified by biomineralization and silk fibroin coating promote bone regeneration in vivo. *Int. J. Biol. Macromol.* **2021**, *172*, 19−29.

(52) Fathyunes, L.; khalili, V. Effect of ultrasonic waves on the electrochemical deposition of calcium phosphate/nano-sized silica composite coating. *J. Mater. Res. Technol.* **2021**, *14*, 2345−2356.

(53) Sadeghi, A.; Moztarzadeh, F.; Mohandesi, J. A. Investigating the effect of chitosan on hydrophilicity and bioactivity of conductive electrospun composite scaffold for neural tissue engineering. *Int. J. Biol. Macromol.* **2019**, *121*, 625−632.

(54) Ran, J.; Hu, J.; Sun, G.; Chen, S.; Chen, L.; Shen, X.; Tong, H. Comparisons between gelatin-tussah silk fibroin/hydroxyapatite and gelatin-Bombyx mori silk fibroin/hydroxyapatite nano-composites for bone tissue engineering. *RSC Adv.* **2015**, *5*, 76526−76537.

(55) Cyran, J. D.; Donovan, M. A.; Vollmer, D.; Brigiano, F. S.; Pezzotti, S.; Galimberti, D. R.; Gaigeot, M. P.; Bonn, M.; Backus, E. H. Molecular hydrophobicity at a macroscopically hydrophilic surface. *Proc. Natl. Acad. Sci. U.S.A.* **2019**, *116*, 1520−1525.

(56) Yan, L. P.; Oliveira, J. M.; Oliveira, A. L.; Caridade, S. G.; Mano, J. F.; Reis, R. L. Macro/microporous silk fibroin scaffolds with potential for articular cartilage and meniscus tissue engineering applications. *Acta Biomater.* **2012**, *8*, 289−301.

(57) Ikeda, T.; Ikeda, K.; Yamamoto, K.; Ishizaki, H.; Yoshizawa, Y.; Yanagiguchi, K.; Yamada, S.; Hayashi, Y. Fabrication and characteristics of chitosan sponge as a tissue engineering scaffold. *BioMed Res. Int.* **2014**, *2014*, No. 786892.

(58) Zhang, Y.; Zhang, M. Synthesis and characterization of macroporous chitosan/calcium phosphate composite scaffolds for tissue engineering. *J. Biomed. Mater. Res.* **2001**, *55*, 304−312.

(59) Li, D.; Tao, L.; Shen, Y.; Sun, B.; Xie, X.; Ke, Q.; Mo, X.; Deng, B. Fabrication of multilayered nanofiber scaffolds with a highly aligned nanofiber yarn for anisotropic tissue regeneration. *ACS Omega* **2020**, *5*, 24340−24350.

(60) Rezvani, M. B.; Atai, M.; Hamze, F.; Hajrezai, R. The effect of silica nanoparticles on the mechanical properties of fiber-reinforced composite resins. *J. Dent. Res., Dent. Clin., Dent. Prospects* **2016**, *10*, No. 112.

(61) Johari, N.; Moroni, L.; Samadikuchaksaraei, A. Tuning the conformation and mechanical properties of silk fibroin hydrogels. *Eur. Polym. J.* **2020**, *134*, No. 109842.

(62) Gali, K. K.; Soundararajan, N.; Katiyar, V.; Sivaprakasam, S. Electrospun chitosan coated polylactic acid nanofiber: a novel immobilization matrix for α−amylase and its application in hydrolysis of cassava fibrous waste. *J. Mater. Res. Technol.* **2021**, *13*, 686−699.

(63) Salim, S. A.; Loutfy, S. A.; El-Fakharany, E. M.; Taha, T. H.; Hussien, Y.; Kamoun, E. A. Influence of chitosan and hydroxyapatite incorporation on properties of electrospun PVA/HA nanofibrous mats for bone tissue regeneration: Nanofibers optimization and in-vitro assessment. *J. Drug Delivery Sci. Technol.* **2021**, *62*, No. 102417.

(64) Dehghani, N.; Haghiralsadat, F.; Yazdian, F.; Sadeghian-Nodoushan, F.; Ghasemi, N.; Mazaheri, F.; Pourmadadi, M.; Naghib, S. M. Chitosan/silk fibroin/nitrogen-doped carbon quantum dot/α-

tricalcium phosphate nanocomposite electrospinned as a scaffold for wound healing application: In vitro and in vivo studies. *Int. J. Biol. Macromol.* **2023**, *238*, No. 124078.

(65) Atay, H. Y.Antibacterial Activity of Chitosan-Based Systems. In *Functional Chitosan*; Springer, 2019; pp 457−489.

(66) Souto-Lopes, M.; Grenho, L.; Manrique, Y. A.; Dias, M. M.; Fernandes, M. H.; Monteiro, F. J.; Salgado, C. L. Full physicochemical and biocompatibility characterization of a supercritical CO2 sterilized nano-hydroxyapatite/chitosan biodegradable scaffold for periodontal bone regeneration. *Biomater. Adv.* **2023**, *146*, No. 213280.

(67) Asiri, A.; Saidin, S.; Sani, M. H.; Al-Ashwal, R. H. Epidermal and fibroblast growth factors incorporated polyvinyl alcohol electrospun nanofibers as biological dressing scaffold. *Sci. Rep.* **2021**, *11*, No. 5634.

(68) Ramanathan, G.; S, L. S. S.; Fardim, P.; Fardim, P.; Sivagnanam, U. T. Fabrication of 3D dual-layered nanofibrous graft loaded with layered double hydroxides and their effects in osteoblastic behavior for bone tissue engineering. *Process Biochem.* **2018**, *64*, 255−259.

(69) Shirosaki, Y.; Tsuru, K.; Hayakawa, S.; Osaka, A.; Lopes, M. A.; Santos, J. D.; Fernandes, M. H. In vitro cytocompatibility of MG63 cells on chitosan-organosiloxane hybrid membranes. *Biomaterials* **2005**, *26*, 485−493.

(70) Rama, M.; Vijayalakshmi, U. Biological and mechanical investigation of novel flax/silk protein-based nanofibrous scaffold for bone regeneration. *Prog. Nat. Sci.: Mater. Int.* **2022**, *32*, 443−455.

(71) Murugapandian, R.; Simona, C.; Vijayalakshmi, U. Fabrication and In Vitro Drug Delivery Evaluation of Cephalexin Monohydrate-Loaded PLA: PVA/HAP: TiO2 Fibrous Scaffolds for Bone Regeneration. *ACS Omega* **2023**, *8*, 5017−5032.

(72) Luraghi, A.; Peri, F.; Moroni, L. Electrospinning for drug delivery applications: A review. *J. Controlled Release* **2021**, *334*, 463−484.

(73) Sivasankarapillai, V. S.; Das, S. S.; Sabir, F.; Sundaramahalingam, M. A.; Colmenares, J. C.; Prasannakumar, S.; Rajan, M.; Rahdar, A.; Kyzas, G. Z. Progress in natural polymer engineered biomaterials for transdermal drug delivery systems. *Mater. Today Chem.* **2021**, *19*, No. 100382.

(74) Farokhi, M.; Mottaghitalab, F.; Reis, R. L.; Ramakrishna, S.; Kundu, S. C. Functionalized silk fibroin nanofibers as drug carriers: Advantages and challenges. *J. Controlled Release* **2020**, *321*, 324−347.

(75) Zeng, Z.; Hu, C.; Liang, Q.; Tang, L.; Cheng, D.; Ruan, C. Coaxial-printed small-diameter polyelectrolyte-based tubes with an electrostatic self-assembly of heparin and YIGSR peptide for antithrombogenicity and endothelialization. *Bioact. Mater.* **2021**, *6*, 1628−1638.

(76) Chen, Y.; Qiu, Y.; Wang, Q.; Li, D.; Hussain, T.; Ke, H.; Wei, Q. Mussel-inspired sandwich-like nanofibers/hydrogel composite with super adhesive, sustained drug release and anti-infection capacity. *Chem. Eng. J.* **2020**, *399*, No. 125668.

(77) Vivek, R.; Thangam, R.; Nipunbabu, V.; Ponraj, T.; Kannan, S. Oxaliplatin-chitosan nanoparticles induced intrinsic apoptotic signaling pathway: a "smart" drug delivery system to breast cancer cell therapy. *Int. J. Biol. Macromol.* **2014**, *65*, 289−297.

(78) Hasanbegloo, K.; Banihashem, S.; Dizaji, B. F.; Bybordi, S.; Farrokh-Eslamlou, N.; Abadi, P. G. S.; Jazi, F. S.; Irani, M. Paclitaxel-loaded liposome-incorporated chitosan (core)/poly (ε-caprolactone)/chitosan (shell) nanofibers for the treatment of breast cancer. *Int. J. Biol. Macromol.* **2023**, *230*, No. 123380.

(79) Ma, K.; Qiu, Y.; Fu, Y.; Ni, Q. Q. Electrospun sandwich configuration nanofibers as transparent membranes for skin care drug delivery systems. *J. Mater. Sci.* **2018**, *53*, 10617−10626.

(80) Al-Baadani, M. A.; Yie, K. H. R.; Al-Bishari, A. M.; Alshobi, B. A.; Zhou, Z.; Fang, K.; Dai, B.; Shen, Y.; Ma, J.; Liu, J.; Shen, X. Co-electrospinning polycaprolactone/gelatin membrane as a tunable drug delivery system for bone tissue regeneration. *Mater. Des.* **2021**, *209*, No. 109962.

(81) Rama, M.; Vijayalakshmi, U. Drug delivery system in bone biology: an evolving platform for bone regeneration and bone infection management. *Polym. Bull.* **2023**, *80*, 7341−7388.

(82) Delan, W. K.; Ali, I. H.; Zakaria, M.; Elsaadany, B.; Fares, A. R.; ElMeshad, A. N.; Mamdouh, W. Investigating the bone regeneration activity of PVA nanofibers scaffolds loaded with simvastatin/chitosan nanoparticles in an induced bone defect rabbit model. *Int. J. Biol. Macromol.* **2022**, *222*, 2399−2413.